MONTE CARLO MODELING OF MULTIPLY SCATTERED LASER CEILOMETER RETURNS

by: Chan W. Keith and Stephen K. Cox

Department of Atmospheric Science
Colorado State University
Fort Collins, CO 80523

Funding Agencies:
National Oceanic and Atmospheric Administration
Grant NAG 1-1146
Office of Naval Research
Contract No. N00014-91-J-1422, P00004

Colorado State University

DEPARTMENT OF ATMOSPHERIC SCIENCE

PAPER NO. 548

MONTE CARLO MODELING OF MULTIPLY SCATTERED LASER CEILOMETER RETURNS

Chan W. Keith and Stephen K. Cox

Department of Atmospheric Science
Colorado State University
Fort Collins, CO 80523

Research Supported By

National Oceanic and Atmospheric Administration (Grant NAG 1-1146)
Office of Naval Research (Contract No. N00014-91-J-1422, P00004)

February, 1994

Atmospheric Science Paper No. 548

ABSTRACT

MONTE CARLO MODELING OF MULTIPLY SCATTERED LASER CEILOMETER RETURNS

Initial analysis of the data from the laser ceilometer used during the First ISCCP (International Satellite Cloud Climatology Project) Regional Experiment (FIRE) and Atlantic Stratocumulus Transition Experiment (ASTEX) programs indicated that clouds were sometimes not reported even though clouds were visible over the ceilometer. In order to understand this inconsistency, a model using Monte Carlo techniques has been refined to study the effect that multiple scattering and other physical processes have on near infrared laser ceilometer returns. The model traces photon paths through three orders of scattering within various scattering media and determines the photon's probability of returning to the receiver at each scattering point. The Monte Carlo model allows for a limited number of horizontal and vertical inhomogeneities in the extinction coefficient and scattering phase function within the scattering media. Clear air and background aerosol scattering, based on published standards are also introduced within the model. Results from the current model are compared with previously published results. Specific atmospheric media and laser ceilometer parameters are modeled, and a factor, α, is defined to measure the effects of each. Results from the model indicate that precipitation and extinction by the subcloud layer have the most significant impact upon the return signal. For clouds with the same optical depth, those with an increasing extinction with depth exhibited a flatter, smaller magnitude return signal than those with a constant or decreasing

extinction. Rayleigh scattering and background aerosols in the subcloud layer decrease the return signal from the cloud and introduce a background level of return from below the cloud. Rain in the subcloud layer lowers the return signal from the cloud, but increases the signal from the subcloud layer due to its relatively large extinction, while realistic levels of absorption have no significant impact. Lastly, a quantitative assessment of detectability for clouds is made, based on α_{min} as a threshold. Model results indicate that conditions can exist where a cloud may not be identified by the laser ceilometer.

ACKNOWLEDGEMENTS

We would like to thank Dr. Thomas B. McKee, Dr. Chiaoyao She, and Dr. John M. Davis for their comments and assistance on this work, and the United States Air Force for providing Chan Keith with this opportunity for graduate study. Lastly, I (Chan Keith) would like to express appreciation to my wife, Tracey, for her support during all of the stages of this research.

This research was supported by The Office of Naval Research under Contract No. N00014-91-J-1422, P00004 and the National Aeronautics and Space Administration under Grant NAG 1-1146.

TABLE OF CONTENTS

CHAPTER 1. INTRODUCTION

Ouldridge, et al (1986) performed an operational comparison of 11 production ceilometers, and demonstrated that there were significant differences in how well each performed. He also determined that all of them had difficulties measuring the cloud base height in specific types of atmospheric media. Although these difficulties can partly be attributed to ceilometer performance, the physical processes that occur within the atmosphere may also be a contributing factor at wavelengths associated with laser ceilometers. The laser ceilometer data obtained during the ASTEX program reflected the difficulties mentioned above. The information produced by the ceilometer suggested that no clouds were present when other evidence indicated the presence of a cloud. It is the objective of this research to further our understanding of how ceilometer performance depends upon the microphysical and radiative properties of the medium into which it is probing.

Laser ceilometers typically measure cloud height by determining the amount of time required for electromagnetic energy to travel from the ceilometer transmitter to the cloud base and down to the receiver, and converting this transit time to height, based on the known speed of energy

propagation. The conversion from measured time to the determination of cloud base height assumes that the returned energy is primarily the result of single scattering; thus multiple scattering effects are neglected. Based on this assumption, the expected amount of returned energy can be determined from the basic lidar equation, (Measures (1983))

$$P_r(r) = P_t \frac{A_r}{r^2} \frac{P(\pi)}{4\pi} \beta_s \frac{\Delta h}{2} \exp\left[-2\int_0^r \beta_e(r')\,dr'\right],$$

where P_r is returned power, P_t is transmitted power, A_r is the receiver area, r is the range, or distance to the scattering point, β_s is the volume scattering coefficient, β_e is the volume extinction coefficient, and Δh is the pulse length. Eloranta (1972) and Kunkel (1974), among others, however, have shown that multiple scattering effects within the atmosphere are not negligible at typical lidar wavelengths, particularly for optically thick media.

In order to simulate the propagation of the transmitted ceilometer pulse through the atmosphere and its reflection by cloud particles, a Monte Carlo radiative transfer model has been developed and applied. This model traces photon paths through the atmosphere, and modeled interactions are based on the probability of that interaction or event actually occurring. A large number of photons are followed to eliminate the statistical uncertainty associated with this method. Lidar and laser ceilometer geometries are

similar, and typical geometry is depicted in Figure 1.1. The scattering medium is located some distance, h, away from the transmitter. The transmitted laser energy is emitted at an elevation angle, usually 90 degrees, with the beam diverging at some half angle, θ_t. The colocated receiver has a field of view of half angle θ_r. The scattering medium has a thickness or depth, d, and extinction coefficient, β_e (in units of inverse length).

A number of authors have reported results for multiple scattering within specific scattering media, and have used this or similar geometry to calculate the effects of multiple scattering on transmitted or backscattered energy. Collins and Wells (1965, 1970) and Collins et al., (1972) developed Monte Carlo code used to study radiative transfer problems, and applied their model to spherical shell atmospheres. Plass and Kattawar (1968a, b, c, 1970) and Kattawar and Plass (1968a, b) applied a Monte Carlo model to determine the effects that changes in the cloud single scattering albedo, particle size distribution, and multiple scattering have on transmitted and reflected solar energy. Plass and Kattawar (1971) also applied their model to typical lidar geometry to calculate the expected returned flux as a function of photon path length and order of scattering. They demonstrated that returns from multiple scattering quickly became more important as the photon path length increased. Liou and Schotland (1971) developed a

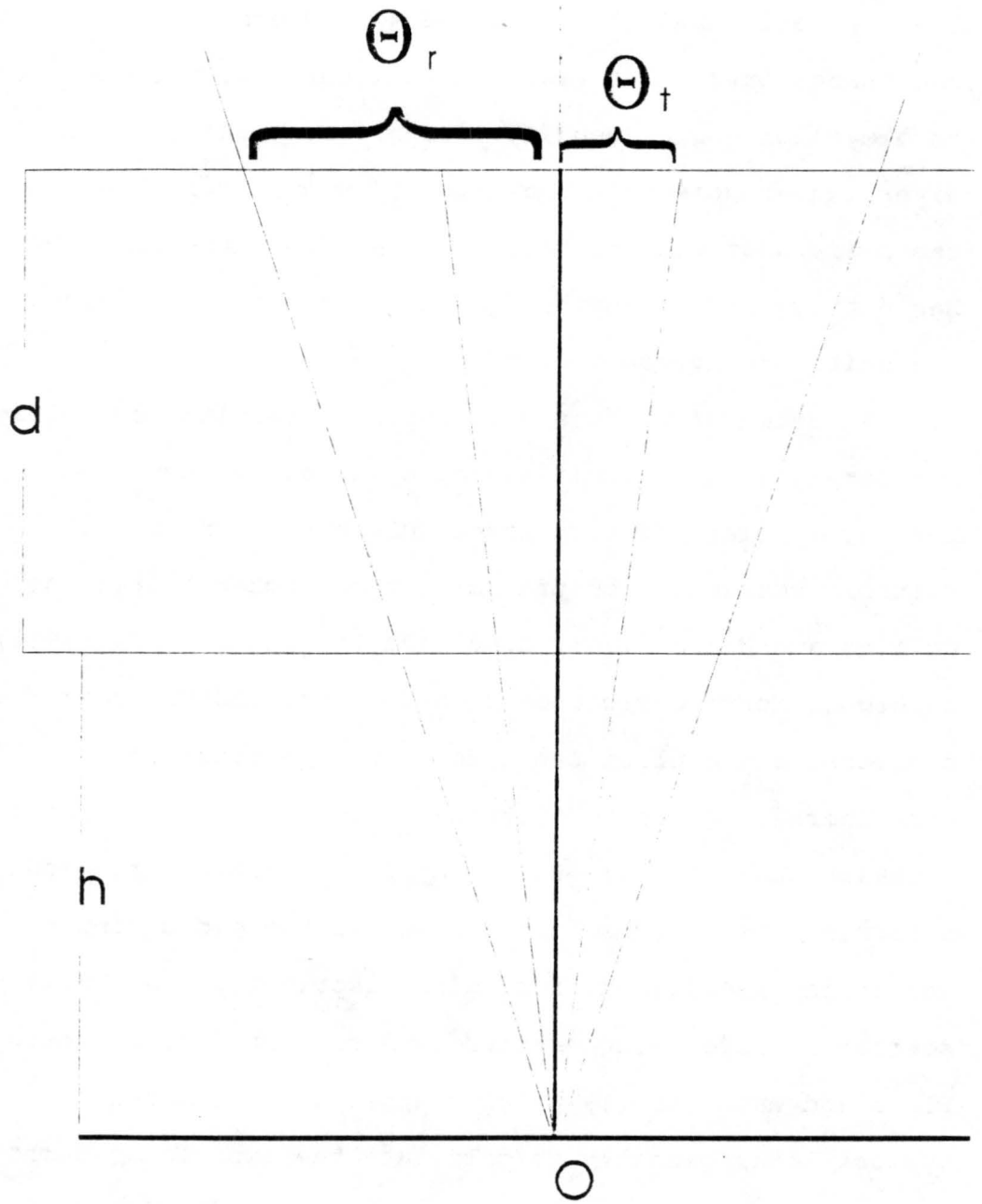

Figure 1.1 Typical lidar and laser ceilometer geometry. Transmitter and receiver are colocated at O. Transmitted beam has divergence of half angle, θ_t, receiver has field of view with half angle, θ_r. β_e is the extinction coefficient for the scattering medium, which is located a distance, h, away from the receiver, and has a depth, d.

computational approach for determining the second order scatter contribution to the returned laser energy for water clouds, based on the geometry of the system. Within their model, clouds were assumed to be homogeneous. Liou (1971) further developed this method to determine the multiple scatter contribution to the overall returned power. Their results predicted that multiple scattering higher than second order would produce a negligible contribution to the overall returned power for water clouds. Eloranta (1972) developed an analytical relationship between the lidar scattering geometry and expected returns from multiple order scattering. His results differed significantly from those of Liou and Schotland. Kunkel (1974) and Kunkel and Weinman (1976) and Weinman (1976) used a Monte Carlo model to determine the effect that multiple scattering has on backscattered lidar energy from homogeneous media, and developed a correction factor, F, to account for the multiple scattering effects. They determined that the correction to the mean extinction coefficient may be as much as 50 percent within particular scattering media. Platt (1981) used a Monte Carlo model to study the effects that multiple scattering within ice crystal clouds have on lidar returns. Predicted multiple scattering contributions from his model compared favorably with those of Eloranta (1972) and Kunkel and Weinman (1976) for specific water clouds. More recently, Bissonnette (1988) and Eichle and Weigner

(1992) developed an analytical approach to determine the impact of multiple scattering on lidar returns.

The model used in the current study is a modified version of a model first established by McKee and Cox (1974, 1976) to simulate the solar radiation field reflected from a finite cubic cloud. It was then used to study solar absorption in finite clouds (Davis, 1979a, b, and McKee et al., 1983). Revisions were made by Davis et al. (1985) to employ a local estimate to investigate problems in visibility, and Weissbluth et al. (1987) and Tsay et al. (1987) used a backward version with spherical shell geometry to further research visibility and spectral contrast problems.

Although the principles surrounding the lidar and the laser ceilometer are very similar, there has been much less modeling work applied directly to laser ceilometers. The change in wavelengths from previous lidar modeling to the current laser ceilometer modeling results in changes to the phase functions for specific cloud types and changes to the extinction coefficient within each of the scattering media.

The purpose of this research is to simulate and analyze the effects that multiple scattering and other physical processes have on laser ceilometer returns. In particular, the following chapters will (a) present a Monte Carlo model used for modeling laser ceilometer returns, (b) compare current model results for lidar specific wavelengths with

results from previous authors, (c) introduce a quantitative parameter, α, and use it to measure laser ceilometer performance, (d) model the physical processes taking place between the transmitted electromagnetic energy and atmospheric media, and (e) determine the performance of a specific laser ceilometer with data obtained from the Atlantic Stratocumulus Transition Experiment (ASTEX) program.

CHAPTER 2. THE MONTE CARLO MODEL

A. General

Monte Carlo modeling has been used extensively in a number of scientific fields, including radiative transfer. The Monte Carlo model is a statistical approach to solving problems such as radiative transfer within the atmosphere. Use of this method requires knowledge of the probability of specific events occurring; this information is represented in the form of probability density functions (PDF). Random numbers are selected and applied to the PDF's to determine the transmittance through the scattering media along a specific photon path, the types of scatter that are allowed to occur, and the direction of scatter for each of the scattering events. Several forms of the Monte Carlo model were available, and, in part, differ by the direction (forward or backward) that the model follows specific photon trajectories. The model used in this work is a forward Monte Carlo model, and follows photons from the transmitter, in the forward direction.

B. Model Procedure and Application

The current model traces each photon path from the transmitter through three successive scatters. Specific laser ceilometer and scattering geometry used in the current

model is depicted in Figure 2.1. The near vertical cloud edges are defined, as in Kunkel (1974) and Platt (1981), such that a horizontal photon path from the vertical or near vertical laser beam axis to the cloud edge must attain an optical depth of at least 0.5. From the transmitter, the photon path has a specific azimuth angle, Φ_0, determined randomly between 0 and 2π, and zenith angle, θ_0, determined randomly, such that $0 \leq \theta_0 \leq \theta_t$, where θ_t is the half angle of the transmitter beam divergence, as defined previously. For each photon departing the transmitter, every angle between the angle limits has an equal probability of being chosen.

A scattering site along the photon path must then be selected. The probability that a photon will travel through a medium without an interaction is determined by

$$PR = e^{-\tau} = \exp\left(-\int_0^s \beta_e ds\right),$$

where τ is the optical depth, β_e is the extinction coefficient, and s is the distance through the medium. To compute the distance along the photon path to each scatter, a random number is chosen for PR, the probability in the equation above, and the upper limit of integration, s, is computed. To make the model computationally more efficient, as in Kunkel and Weinman (1976), Plass and Kattawar (1971), and Platt (1981), each photon is forced to scatter within the scattering medium. The probability of the photon

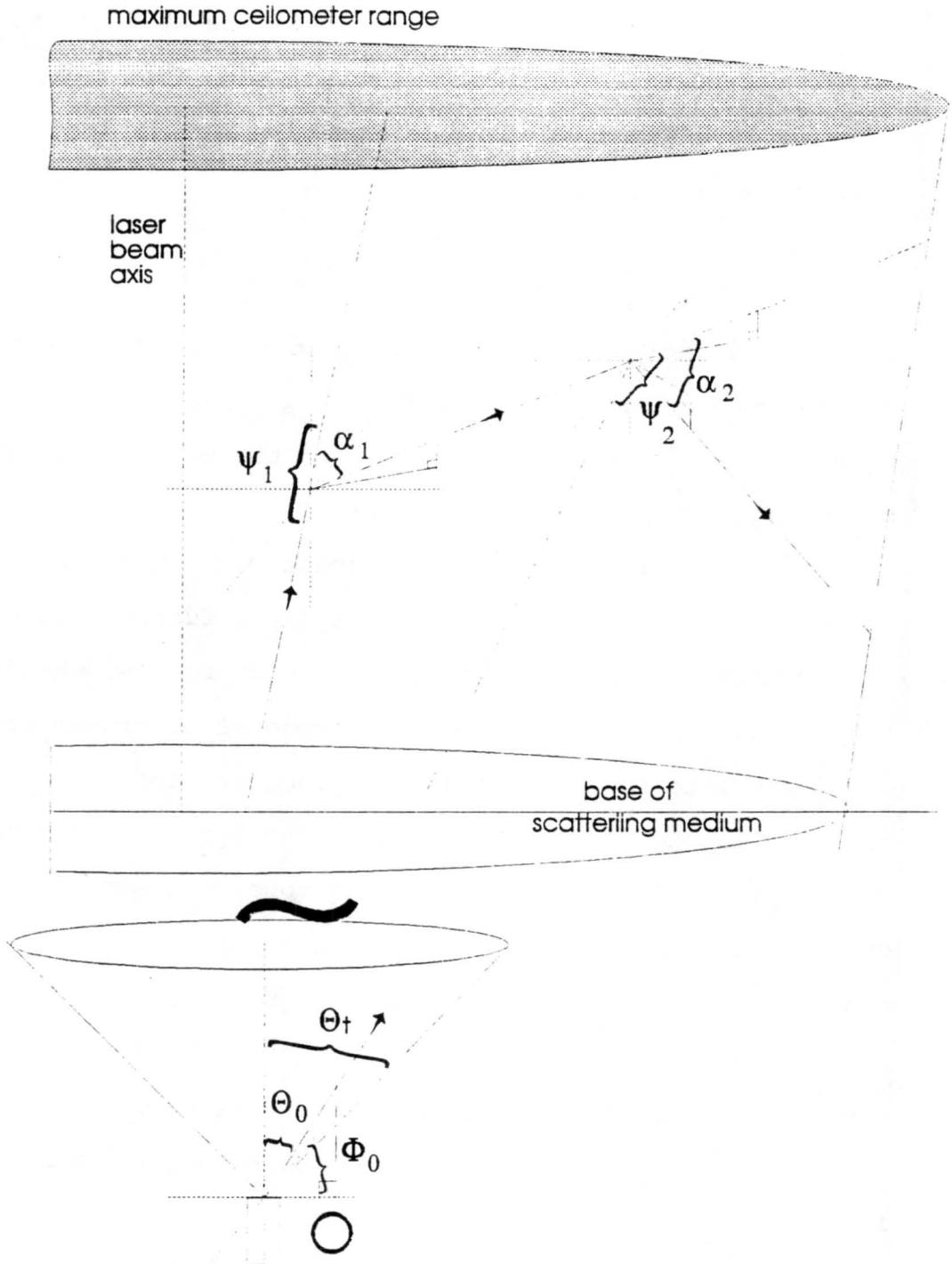

Figure 2.1. Ceilometer and scattering geometry used in the current model. The ceilometer transmitter and receiver are located at position O. Specific geometry parameters are defined in the text.

reaching the detector, which is directly related to the backscattered energy, is suitably reduced. The distance, S_i, from each starting point to each scattering site can then be calculated as

$$S_i = \frac{1}{\beta_e}(-\ln(1-RN(1-T_i))),$$

where β_e is the extinction coefficient for the photon path, RN is a random number between 0 and 1, and T_i is the transmittance from the starting point to the model boundary along the photon path.

The constituent causing the scatter is then determined. The constituent type determines the phase function to be used within some of the calculations that follow. Rayleigh, background aerosol, and up to two types of other aerosol scattering, to include clouds and precipitation, are possible in the model. This scattering type is determined randomly, and is weighted according to each constituent's contribution to the total extinction coefficient. Rayleigh and background aerosol concentrations used in this work are based on published tables (Elterman, 1968). The phase function for the background aerosol in the current model was approximated by the phase function for Haze L (Diermendjian, 1969, 1975).

At each scattering site, the probability of the photon returning to the receiver directly is computed as

$$PS = \left[\frac{A_{eff} P(\psi)}{z^2}\right] W_n \omega_0^n \exp\left[-\sum_{i=1}^{i=m} \beta_{e_i} (z_{i-1} - z_i)\right],$$

where A_{eff} is the effective receiver aperture, $P(\Psi)$ is the applicable single scattering phase function for the angle, Ψ, z is the distance from the scattering point to the receiver, m is the number of inhomogeneous media physically between the scattering site and the receiver, and z_0 is the height of the scattering site, ω_0 is the single scattering albedo of the medium, and n is the order of scatter. W_n is a weighting factor to compensate for forcing the scatters to occur within the scattering media, and is computed as

$$W_n = (1 - \tau_n) W_{n-1},$$

where τ_n is the optical depth through the scattering medium, from the starting point to the scattering point, for each order of scattering, n. W_0 is 1.00.

At each scattering site, a new direction is determined by randomly choosing the scattering angle, α_n, defined as the angle between the old direction vector and the new direction vector, within the plane of the two vectors. The random selection is appropriately weighted based on the normalized single scattering phase function of the scattering medium. Since the scattering constituents are symmetric about the old vector, the new azimuth angle, determined from the photon's frame of reference, is chosen randomly between 0 and 2π.

After three scattering sites and probabilities are computed, the sum of these probabilities for all photons, as a function of height and order of scattering, is maintained. After all photons are processed, the overall probability of returning to the receiver can be determined.

B. Statistical Convergence.

Model results were tested to ensure a sufficient number of photons were used to provide results that were statistically representative of the overall population. Each of the model runs, comprised of N photons, was divided into 10 equal sets of photons. A mean scattering probability was computed for each of the ten sets and for the entire run, (1) for the entire range of the modeled ceilometer, and (2) at specified depths within the primary scattering medium. The variance for each model run was computed as

$$\sigma^2=\sum_{i=1}^{M}\frac{(x_i-\mu)^2}{M},$$

where X_i is the mean scattering probability of returning to the receiver after scattering, for each set of photons, μ is the mean scattering probability of returning to the receiver after scattering, for the entire run, and M is the number of sets within each run. A sample of the variance for each run, as a function of the number of photons per set is depicted in Figure 2.2. It demonstrates, as the central limit theorem of statistical probability theory predicts, that the

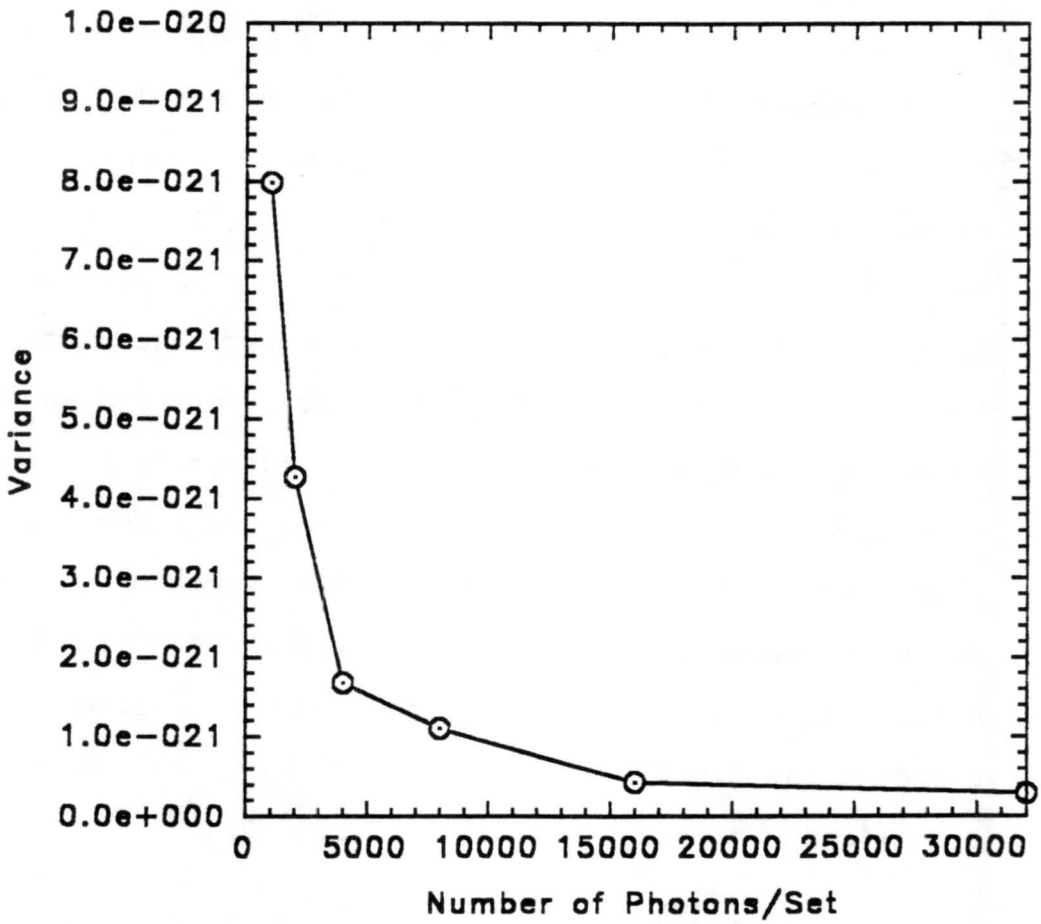

Figure 2.2. Variance of the mean scattering probability for the range of the ceilometer, σ^2, as a function of the number of photons per set, for model runs of 10 sets of photons. Scattering media is Haze L. The extinction coefficeint, β_e, is 10 km^{-1}. The scattering medium has a depth of 1 km, and is located 1 km above the ceilometer.

accuracy of the runs improves by a factor of $1/N^{1/2}$. The normalized standard error was also computed for each of the model runs as

$$Err=\frac{\sqrt{\sigma^2}}{\mu}.$$

Figures 2.3 and 2.4 present calculated errors as a function of the number of photons per set. In these model runs, no scattering or absorption was allowed above or below the cloud. The modeled cloud was a cloud type C.1, defined, as in Deirmendjian (1969), as a cumulus cloud with liquid water content of 0.063 g m^{-3}. Specific parameters are listed in Table 2.1. Figure 2.3 depicts the error over the entire range of a modeled ceilometer, as a function of the number of photons per set. Figure 2.4 depicts the error for specified depths within the cloud, as a function of the number of photons per set. Figure 2.5 and 2.6 present similar results, respectively, for Haze L, defined, as in Deirmendjian (1969), as a continental-type aerosol haze. Specific parameters are listed in Table 2.1.

Table 2.1. Particle size distribution parameters defining specific scattering medium types used in this chapter.

Cloud Type	Deirmendjian Cloud Parameters			
	a	α	γ	r_c (μm)
Nimbostratus, NS	1.10	1.00	2.41	9.67
Cumulus, C.1	2.373	6.00	1.00	4.00
Layered Haze, HzL	4.98×10^6	2.00	0.50	0.07

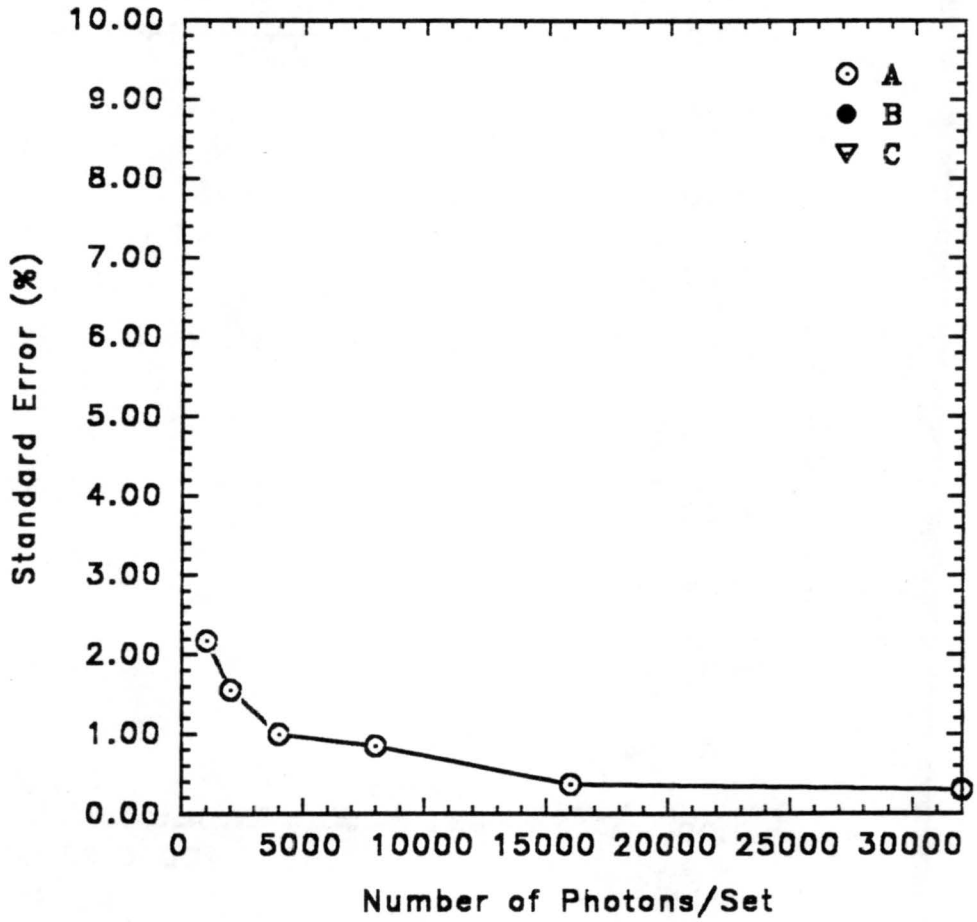

Figure 2.3. Standard error of the mean scattering probability for the range of the ceilometer, as a function of the number of photons per set, for model runs of 10 sets of photons. Scattering medium is cloud C.1. The extinction coefficient is 10 km^{-1}. The scattering medium is 1 km thick, and is located 1 km above the ceilometer.

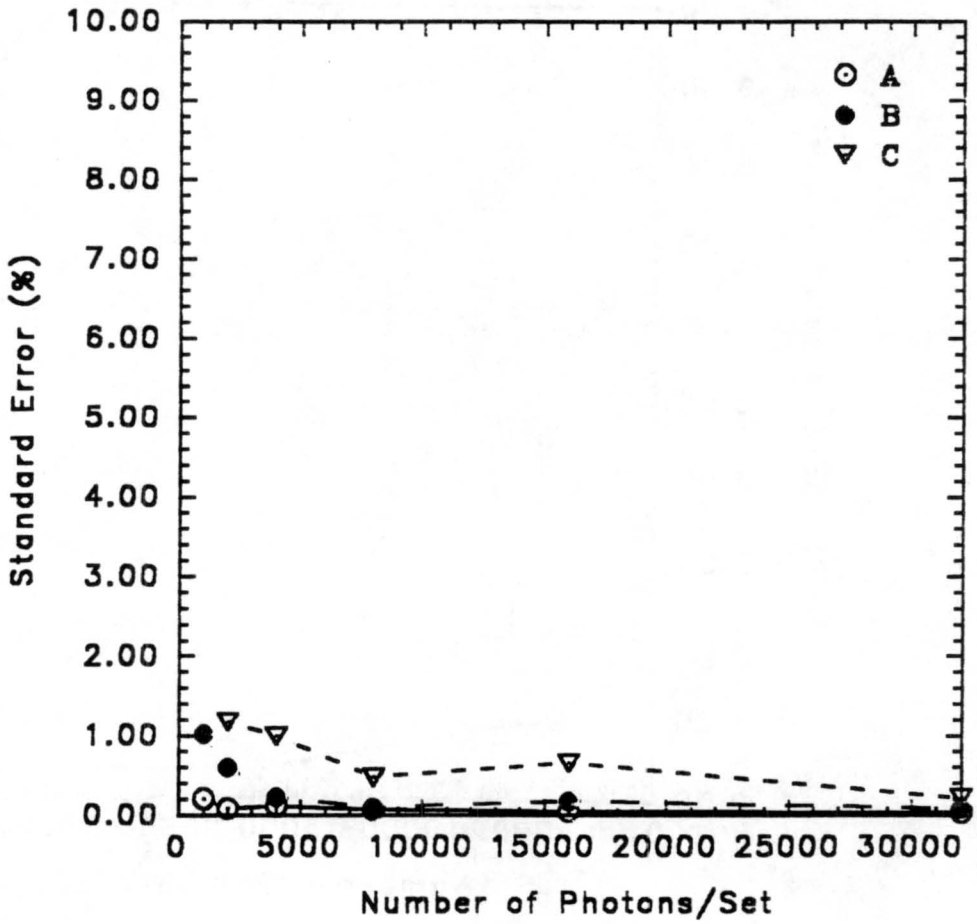

Figure 2.4. Standard error of the mean scattering probability for specific ranges of the modeled ceilometer. Range bin A corresponds to 0-3.2 m into the scattering medium, B corresponds to 170.4-178.0 m into the scattering medium, and C corresponds to the range 360.4-368.0 m into the medium. Cloud type is cloud C.1, located 1 km above the ceilometer, with a depth of 1 km.

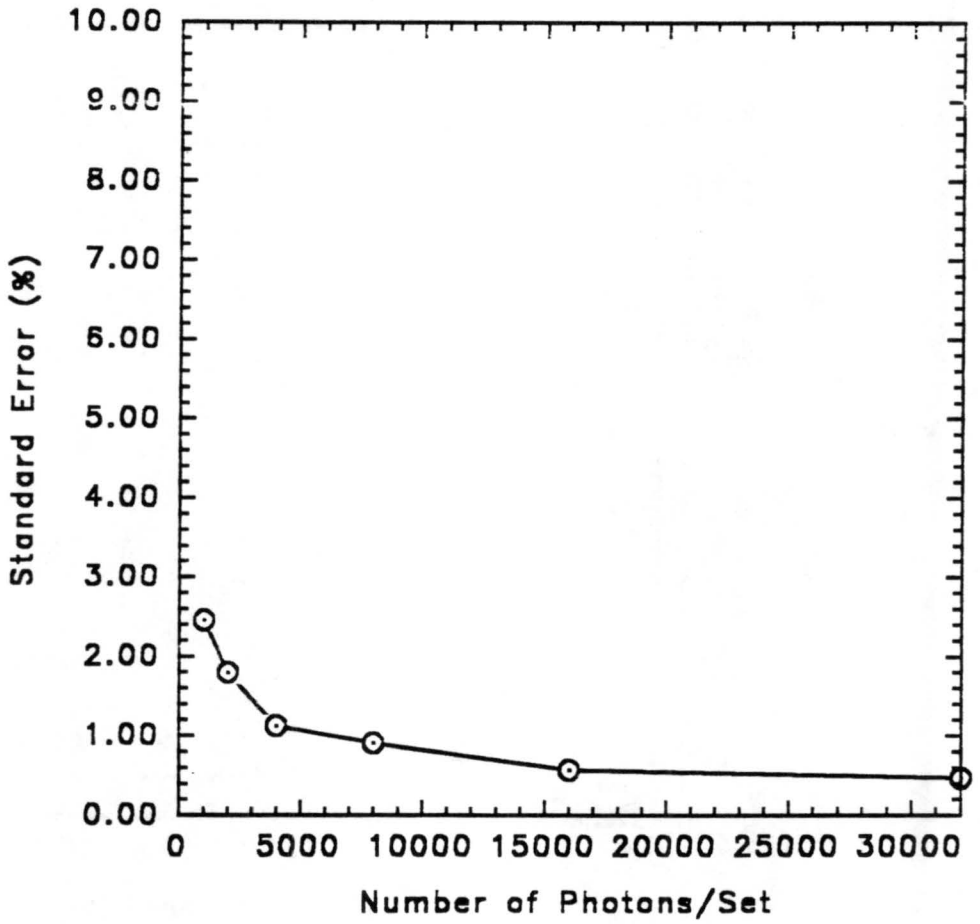

Figure 2.5. As in Figure 2.3, except for scattering medium, Haze L. The scattering medium is located 1 km above the ceilometer, has a depth of 1 km, and extinction coefficient is 10 km^{-1}.

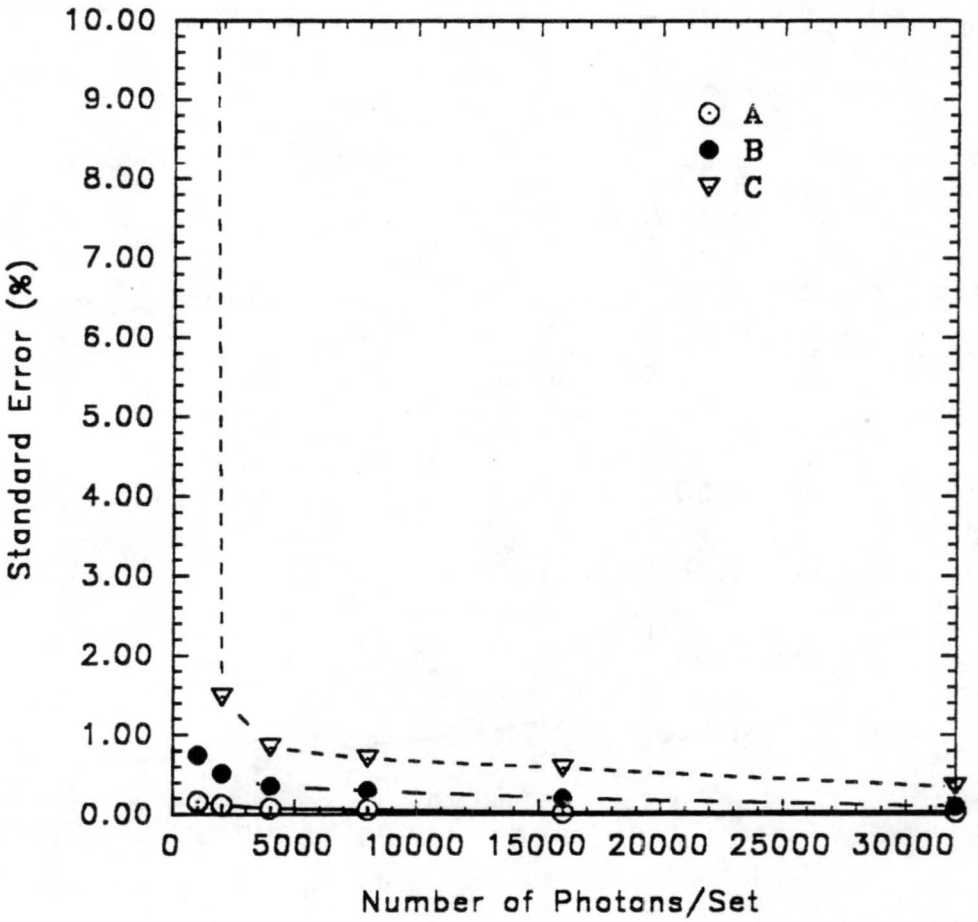

Figure 2.6. As in Figure 2.4, except for scattering medium, Haze L. The scattering medium is located 1 km above the ceilometer, has a depth of 1 km, and extinction coefficient is 10 km^{-1}.

During actual model runs, the appropriate number of photons was selected such that the error of individual bins within an optical depth of five in the primary scattering medium did not exceed 5 percent. This optical depth accounted for over 99 percent of the energy emitted, and effectively minimized statistical scatter in the results.

C. Comparison with Previous Results.

A number of other researchers have tested similar Monte Carlo models using lidar wavelengths near 0.70 microns and a homogeneous scattering medium located a distance, Z_0, away from the colocated transmitter and receiver. Specific parameters used by the previous authors, and within the current model for comparison purposes, are presented in Table 2.2. Particle size distributions are presented in Figures 2.7 and 2.8, and in Table 2.1. As in Diermendjian (1969), the current model uses a modified gamma particle size distribution. The other authors use a different distribution. This difference altered the phase function information within the comparisons, resulting in two slightly different phase functions in the first comparison. In the second comparison, the phase function used by Kunkel was also used in the current model.

Figure 2.9 shows the comparison between the current model results and those of Plass and Kattawar (1971) for a nimbostratus cloud type. The figure presents normalized returned flux as a function of height and multiple

Table 2.2. Specific model parameters used by previous authors and within the current model for comparison purposes.

Modeler	Cloud Type	Cloud Ext. Coeff β_e km^{-1}	Rayleigh and Aerosol Scatter	Cloud Height Z_0 km	Laser Beam Divergence θ_t (mrad)	Receiver Field of View θ_r (mrad)	Receiver Half Angle Defining Cloud Edges θ_m (mrad)
Plass and Kattawar (1971)	NS	10.0	No	1.0	1.00	5.00	
Kunkel (1974)	HazeC	10.0	No	1.0	0.00	5.00	85.0
Current Model	NS TOP	10.0	No	1.0	1.00	5.00	85.0
	HazeL	10.0	No	1.0	0.00	5.00	85.0

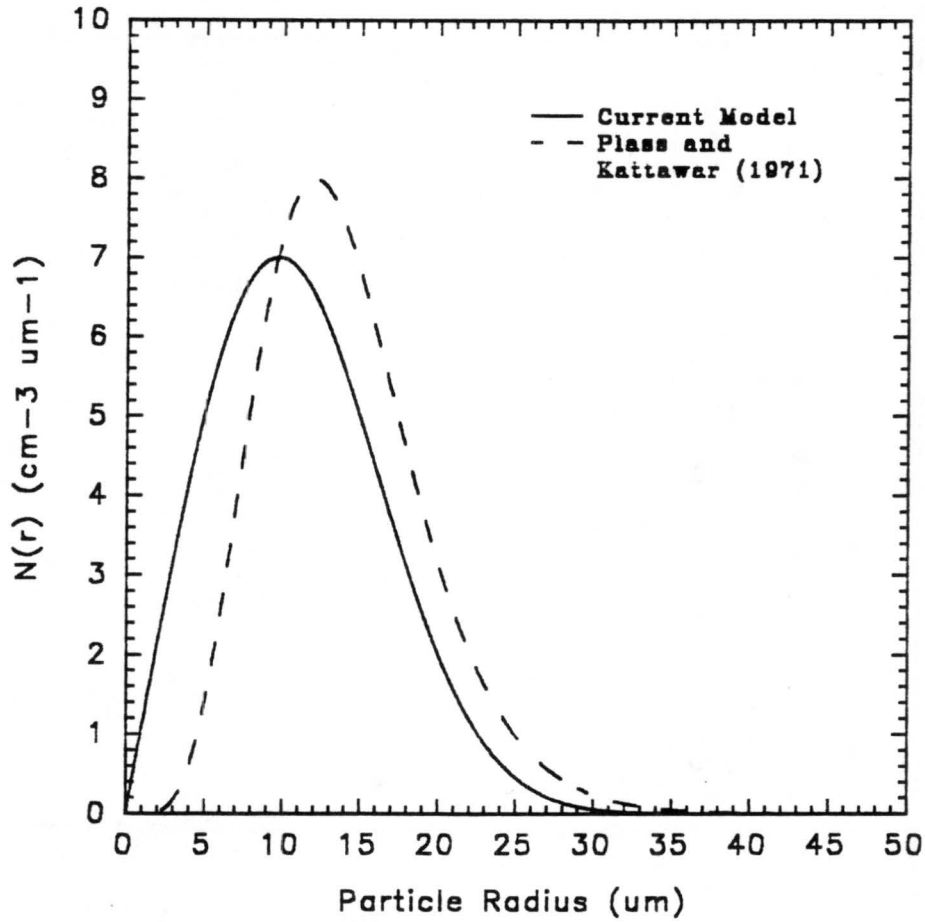

Figure 2.7. Particle size distributions within the scattering media used in the model comparison with Plass and Kattawar (1971). Size distributions are based on a modified gamma distribution for the current model.

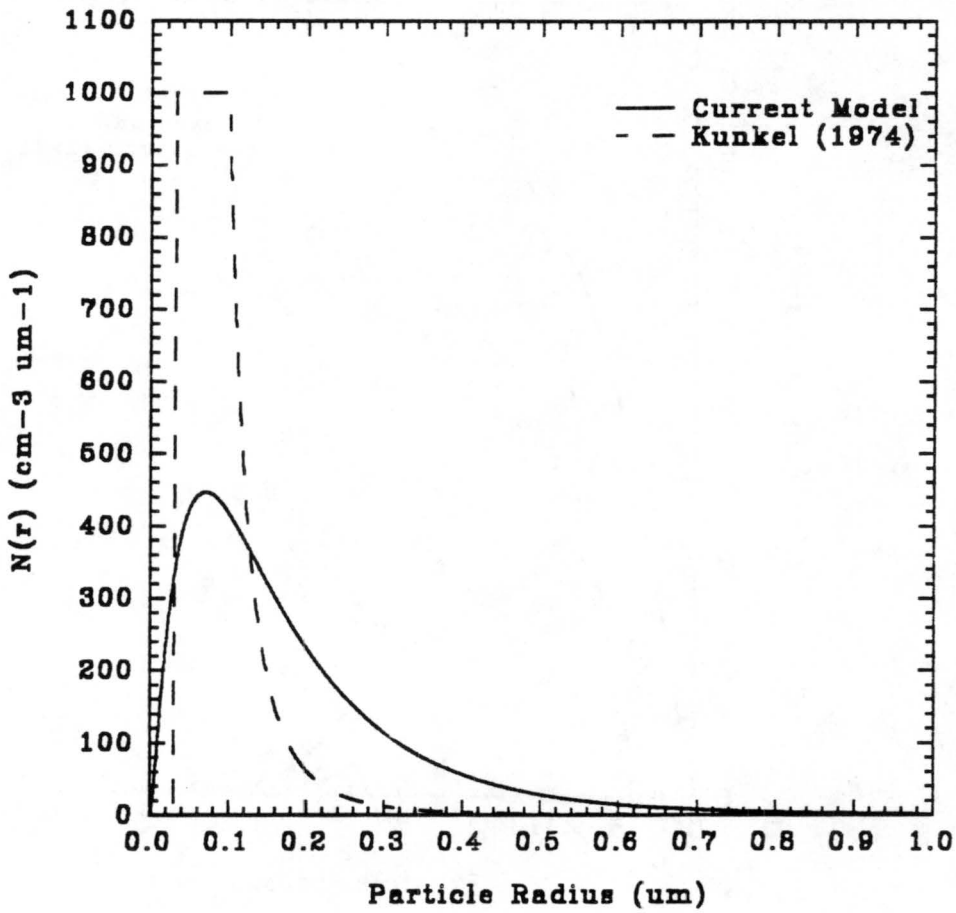

Figure 2.8. Particle size distributions within the scattering media used in the model comparison with Kunkel (1974). Size distributions are based on a modified gamma distribution for the current model.

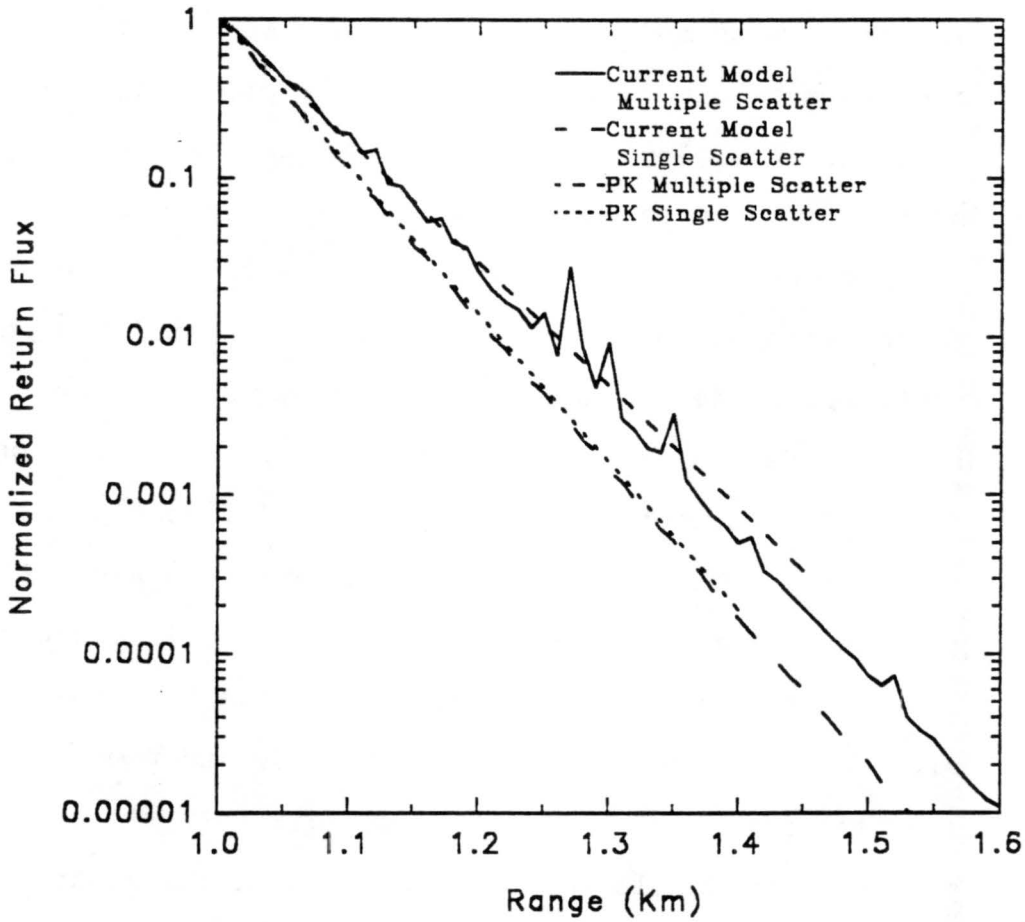

Figure 2.9. Current model results versus those of Plass and Kattawar (1971) for the nimbostratus cloud type. Scattering occurred only within the cloud, located 1 km above the ceilometer.

scattering. The published results of Plass and Kattawar and results from the current model were normalized to compensate for potential differences in the effective area of the receiver and other constants in the computations. As the figure demonstrates, the current results agree quite favorably with model results of Plass and Kattawar. The results show minor differences on the order of a few percent well into the cloud. The difference can be explained by the slight differences in the models. Plass and Kattawar, in their computation of returned flux due to multiple scatter, forced each photon to scatter repeatedly until the photon's contribution fell below some constant, which allowed 4th and higher orders of scattering to contribute to the return flux. The current model limits orders of scattering to 3.

Results from the current model were compared with the results of Kunkel (1974), and Eloranta's (1972) analytical model using the Haze C variables in Table 2.1, the particle size distributions shown in Figure 2.8, and the phase function information given in appendix A-1. Figure 2.10 presents the double scatter return to single scatter return ratio as a function of depth within the scattering medium. The current model shows excellent agreement with the Monte Carlo model results of Kunkel (1974) for Haze C. Variation between the two models' results is less than 5.0 percent overall, and did not exceed 15 percent for any penetration depth within the cloud. The current model predicts the

double scatter to single scatter ratio to be approximately 15 percent less than the analytical model of Eloranta (1972) at the larger optical depths, as did the model of Kunkel (1974).

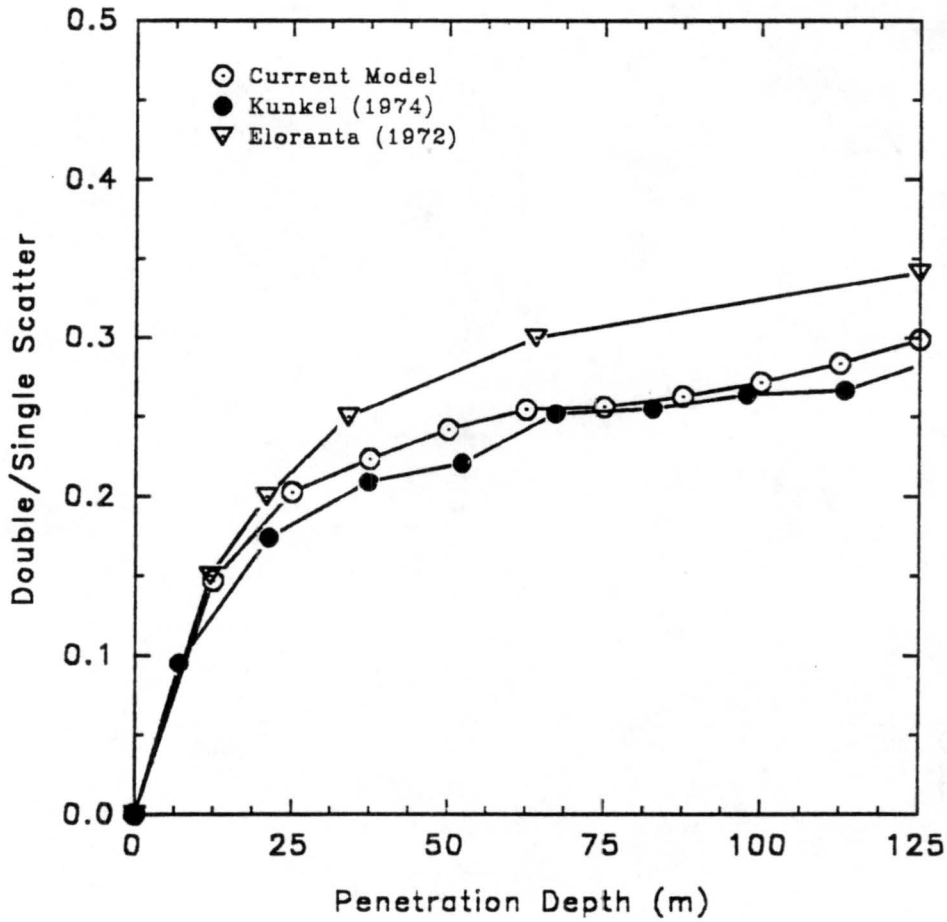

Figure 2.10. Current model results versus the analytical predictions of Eloranta (1972), and the Monte Carlo results of Kunkel (1974), for Haze C. The particle size distributions are in Figure 2.8. The scattering medium is 1 km above the ceilometer, and has a depth of 1 km. Extinction coefficient is 10 km^{-1}.

CHAPTER 3. INITIALIZATION PARAMETERS

A. General

The model results presented in the following chapters are based on specific initialization information. These initialization variables can be loosely divided into two categories: (a) hardware and hardware geometry, and (b) clouds and scattering media parameters. Several assumptions must be made prior to providing the initialization parameters.

In all of the model runs, unless otherwise specified, a vertically pointing ceilometer is assumed. The laser transmits at a wavelength, λ, of 0.90 μm. The pulse width of the transmitted energy results in each range gate having a width of 10.0 m. Unless otherwise specified, the transmitter and receiver are colocated, and are 1 meter above the ground, which is 100 meters above mean sea level. The receiver field of view half angle and transmitter beam divergence half angle are varied for the model runs.

Up to three cloud types or scattering media, not including Rayleigh scattering, was specified for each model run. The heights and thicknesses of each of the scattering media were specified. The single scattering albedo, ω_0, the single scattering phase functions, $P(\psi)$, and the extinction

coefficients, β_e, for specific cloud types are determined by a separate Mie program (Eric A. Smith, Dept. of Atmospheric Science, Colorado State University, Fort Collins, CO) and provided within the model. Phase functions for specific cloud types are depicted in Figures 3.1 and 3.2, and individual values are listed in appendix A.2.

Cloud drop size distributions were based on the modified gamma distribution given by Deirmendjian (1969, 1975) in the form:

$$n(r) = ar^{\alpha}\exp\left[-\frac{\alpha}{\gamma}\left(\frac{r}{r_c}\right)^{\gamma}\right]$$

where n(r), expressed in cm^{-3} μm^{-1}, is the number density of droplets with radius r, and r_c is the modal radius. The parameters, a, α, and γ are empirically derived constants, and are depicted in Table 3.1 for the cloud types used.

Table 3.1. Drop size distribution parameters used for determining cloud radiative transfer functions. Cloud particle size distributions are assumed to have a modified gamma distribution.

Cloud Type	Diermendjian Cloud Parameters			
	a	α	γ	r_c (μm)
Nimbostratus Top (NST)	1.10	1.00	2.41	9.67
Nimbostratus Base (NSB)	8.06×10^{-2}	5.00	1.24	6.41
Stratus Top (STT)	3.82×10^{-1}	3.00	1.30	6.75
Stratus Base (STB)	9.79×10^{-1}	5.00	1.05	4.70
Cumulus (C.1)	2.37	6.00	1.00	4.00
Haze, Layered (HZL)	4.98×10^{6}	2.00	0.50	0.07

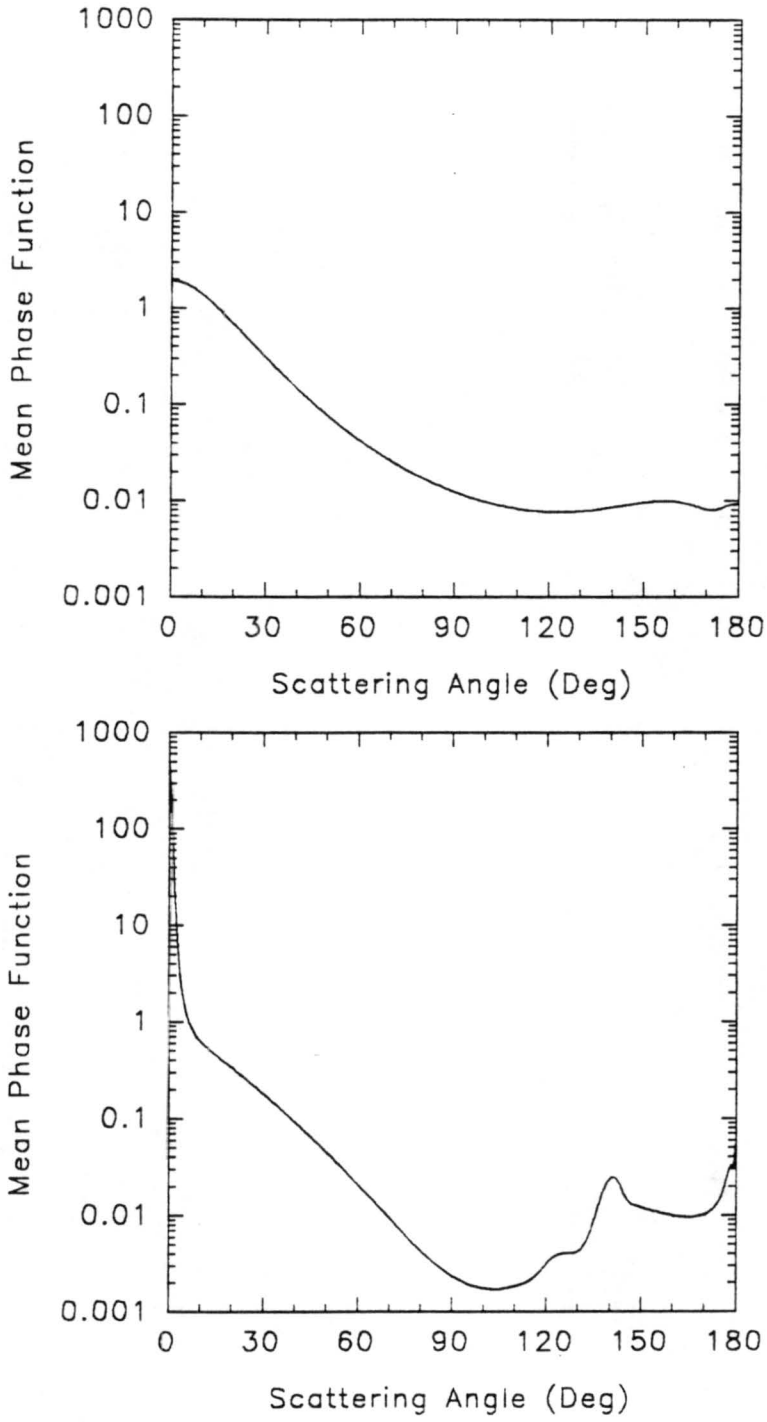

Figure 3.1. Phase functions, $P(\theta)$, as a function of scattering angle, for (a) Haze L, which was used to approximate background aerosol scattering, and (b) Nimbostratus (NS) cloud type.

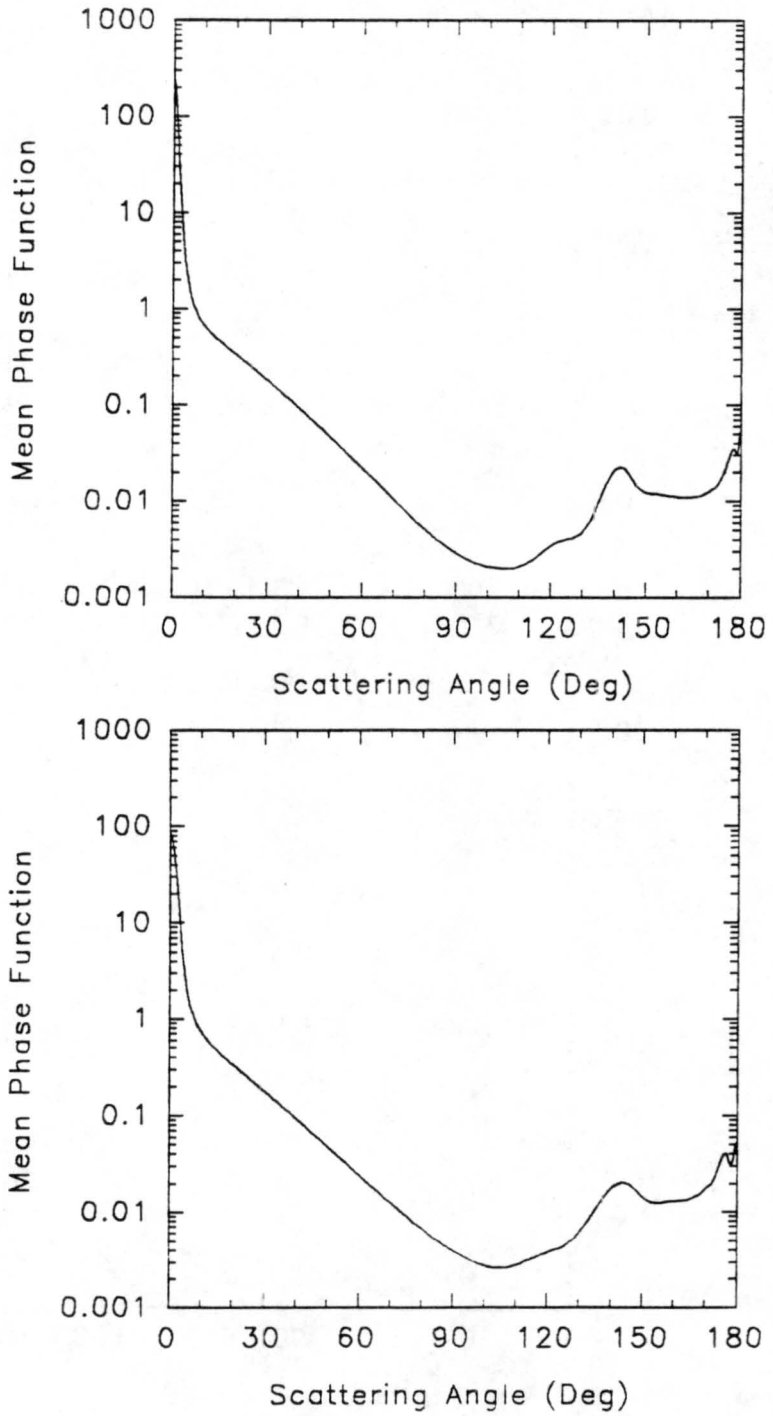

Figure 3.2. Phase functions, $P(\theta)$, as a function of scattering angle, for (a) Stratus (ST), and (b) Cumulus (C.1) cloud types.

To determine the effect that specific processes have on the ceilometer return, it was necessary to run the model a large number of times and vary the input parameters for each run. The runs were divided into groups, where each group of runs consisted of a series of similar model runs, with the cloud type and phase function varied between the runs. The structure of the atmosphere within each group of runs remained constant. The model's initialization variables were configured to assess the influence of several factors on the returned signal of the ceilometer. The factors investigated and the groups of model runs designed to investigate each are: vertical structure of extinction within cloud - groups 2, 3, 4, 5; effects of absorption - groups 6 and 7; subcloud layer extinction - groups 8, 9, 10; effects of precipitation - groups 11 and 12. Group 1 was the control. The objectives and initialization parameters for each of the groups are summarized in Tables 3.2 and 3.3.

B. Effects of cloud structure

Several groups of runs were made to identify how the cloud structure affected the ceilometer return. In all of these groups, a cloud was placed 1 km above the transmitter, and had a depth of 1 km. The single scattering albedo within the cloud was 1.0, and no Rayleigh or background aerosol scattering was allowed. The total optical depth for each of the given cloud types remained constant within all of the groups in this section. The vertical structure of

Table 3.2. Specific input parameters for the groups of runs used within the current Monte Carlo model, based on standard liquid water contents.

Cloud Type	Objective	Extinction Coefficient by layer β_e (Km^{-1})	Opt. Depth τ	Rayleigh and Bkgd Aerosol	Scatt. Albedo ω_0	Cloud LWC ($g\ m^{-3}$)
Grp 1	Control					
NSM		70.0	70.0	No	1.000	0.6344
STM		35.0	35.0	No	1.000	0.2445
C.1		17.0	17.0	No	1.000	0.0626
Grp 2	Cloud					
NSM	Structure	7.0, 21.0, 35.0, 49.0, 63.0, 77.0, 91.0,105.0,119.0,133.0	70.0	No	1.000	Same
STM		3.5, 10.5, 17.5, 24.5, 31.5, 38.5, 45.5, 52.5, 59.5, 66.5	35.0	No	1.000	as
C.1		1.7, 5.1, 8.5, 11.9, 15.3, 18.7, 22.1, 25.5, 28.9, 32.3	17.0	No	1.000	Gp 1
Grp 3	Cloud					
STM	Structure	66.5, 59.5, 52.5, 45.5, 38.5, 31.5, 24.5, 17.5, 10.5, 3.5	35.0	No	1.000	Same as
C.1		32.3, 28.9, 25.5, 22.1, 18.7, 15.3, 11.9, 8.5, 5.1, 1.7	17.0	No	1.000	Gp 1
Grp 4	Cloud					
STM	Structure	10.5, 22.8, 35.0, 47.2, 59.5, 59.5, 47.2, 35.0, 22.8, 10.5	35.0	No	1.000	Same as
C.1		5.1, 11.0, 17.0, 23.0, 28.9, 28.9, 23.0, 17.0, 11.0, 5.1	17.0	No	1.000	Gp 1
Grp 5	Cloud					
STM	Structure	87.5, 87.5, 0.0, 0.0, 0.0, 0.0, 0.0, 0.0, 87.5, 87.5	35.0	No	1.000	Same as
C.1		42.5, 42.5, 0.0, 0.0, 0.0, 0.0, 0.0, 0.0, 42.5, 42.5	17.0	No	1.000	Gp 1

Table 3.2 (continued). Specific input parameters for the groups of runs used within the current Monte Carlo model, based on standard liquid water contents.

Cloud Type	Objective	Extinction Coefficient by layer β_e (Km^{-1})		Opt. Depth τ	Rayleigh and Bkgd Aerosol	Scatt. Albedo, ω_0	Cloud LWC ($g\ m^{-3}$)
Grp 6	Absorption						
STM		35.0		35.0	No	0.990	Same as
C.1		17.0		17.0	No	0.990	Gp1
Gp 13	Precip.	Rain	Cloud				
STB		2.1	35.0	37.1	Yes	1.000	Same as
C.1		2.1	17.0	19.1	Yes	1.000	Gp 1
Gp 14	Precip.	Rain	Cloud				
STB		2.1	35.0	37.1	Yes	0.990	Same as
C.1		2.1	17.0	19.1	Yes	0.990	Gp 1

Table 3.3. Specific input parameters for the groups of runs used within the current Monte Carlo model, based on 1/3 of the standard liquid water contents.

Cloud Type	Objective	Extinction Coefficient by layer β_e (Km^{-1})	Opt. Depth τ	Rayleigh and Bkgd Aerosol	Scatt. Albedo ω_0	Cloud LWC ($g\ m^{-3}$)
Grp 1	Control					
STB		7.7	7.7	No	1.000	0.0350
C.1		5.4	5.4	No	1.000	0.0200
Grp 2	Cloud					
STB	Structure	0.8, 2.3, 3.8, 5.4, 6.9, 8.5, 10.0, 11.6, 13.1, 14.6	7.7	No	1.000	Same as
C.1		0.5, 1.6, 2.7, 3.8, 4.9, 5.9, 7.0, 8.1, 9.2, 10.3	5.4	No	1.000	Gp 1
Grp 6	Absorption					
STB		7.7	7.7	No	0.990	Same as
C.1		5.4	5.4	No	0.990	Gp 1
Grp 7	Absorption					
STB		7.7	7.7	No	0.800	Same as
C.1		5.4	5.4	No	0.800	Gp 1
Grp 8	Subcloud					
STB	Layer	7.7	7.7	Yes	1.000	Same as
C.1	Extinction	5.4	5.4	Yes	1.000	Gp 1
Grp 9	Subcloud					
STB	Layer Extinction	0.8, 2.3, 3.8, 5.4, 6.9, 8.5, 10.0, 11.6, 13.1, 14.6	7.7	Yes	1.000	Same as
C.1		0.5, 1.6, 2.7, 3.8, 4.9, 5.9, 7.0, 8.1, 9.2, 10.3	5.4	Yes	1.000	Gp 1
Gp 10	Subcloud					
STB	Layer	7.7	7.7	Yes	0.990	Same as
C.1	Extinction	5.4	5.4	Yes	0.990	Gp 1

Table 3.3 (continued). Specific input parameters for the groups of runs used within the current Monte Carlo model, based on 1/3 of the standard liquid water contents.

Cloud Type	Objective	Extinction Coefficient by layer β_e (Km^{-1})	Opt. Depth τ	Rayleigh and Bkgd Aerosol	Scat. Albedo, ω_0	Cloud LWC ($g\ m^{-3}$)
Gp 11	Subcloud					
STB	Layer Extinction	0.8, 2.3, 3.8, 5.4, 6.9, 8.5, 10.0, 11.6, 13.1, 14.6	7.7	5 x Std	1.000	Same as
C.1		0.5, 1.6, 2.7, 3.8, 4.9, 5.9, 7.0, 8.1, 9.2, 10.3	5.4	5 x Std	1.000	Gp 1
Gp 12	Subcloud					
STB	Layer Extinction	0.8, 2.3, 3.8, 5.4, 6.9, 8.5, 10.0, 11.6, 13.1, 14.6	7.7	10 x Std	1.000	Same as
C.1		0.5, 1.6, 2.7, 3.8, 4.9, 5.9, 7.0, 8.1, 9.2, 10.3	5.4	10 x Std	1.000	Gp 1
Gp 13	Precip.	Rain / Cloud				
STB		2.1 / 7.7	9.8	Yes	1.000	Same as
C.1		2.1 / 5.4	7.5	Yes	1.000	Gp 1
Gp 14	Precip.	Rain / Cloud				
STB		2.1 / 7.7	9.8	Yes	0.990	Same as
C.1		2.1 / 5.4	7.5	Yes	0.990	Gp 1
Gp 15	Precip.	Rain / Cloud				
STB		2.1 / 7.7	9.8	No	1.000	Same as
C.1		2.1 / 5.4	7.5	No	1.000	Gp 1

the extintion coefficients for the clouds within the groups of this section are summarized in Figures 3.3 and 3.4. Two control groups were established. In group 1a, a single homogeneous cloud was placed within the atmosphere. Three different cloud types were used in separate runs within this group, nimbostratus (NS), stratus (ST) and cumulus (C.1). Specific drop size distributions, liquid water content, extinction coefficients, and optical depths are given in Table 3.2. Group 1b contained the same parameters as group 1a, except the volume extinction coefficient used was based on a liquid water content which was 1/3 that used for group 1a. Parameters defining this control group and the groups that parallel it are in Table 3.3. All of the other groups were established based on these two control groups. The clouds in group 2 were each divided into 10 equal layers. The total optical depth of the cloud remained constant with that of group 1, however, the extinction coefficient increased stepwise with depth into the cloud. Group 2 was modeled using extinction information from each of the control groups. Group 3 clouds were similiar to group 2 except that they had a decreasing stepwise extinction coefficient through the cloud. In group 4, the maximum extinction was within the center of the cloud, and it decreased stepwise toward the cloud edges. Group 5 clouds had an extinction coefficient of 0 km^{-1} within the center portion of the cloud.

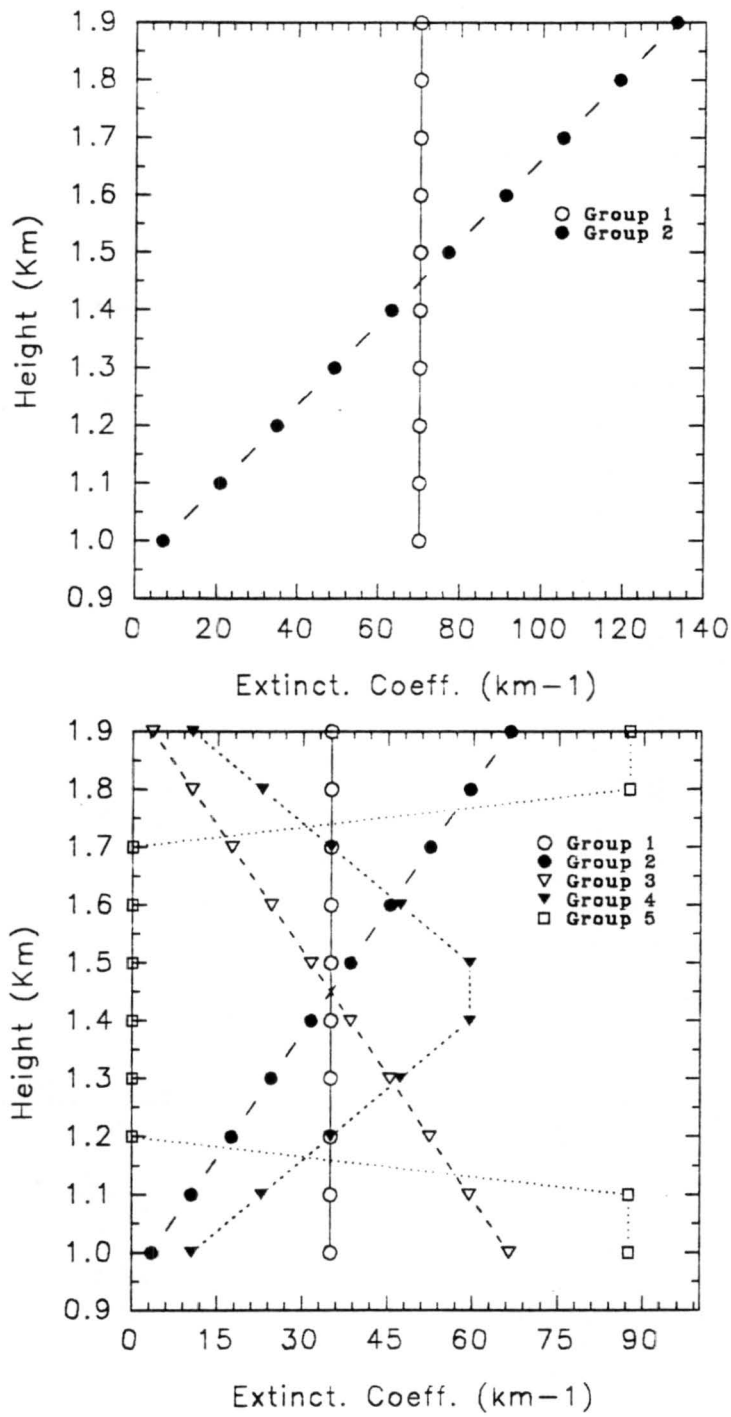

Figure 3.3(a)-(b). Vertical structure of the extinction coefficient within the cloud for Groups 1a-5a, for (a) NS, and (b) ST cloud types.

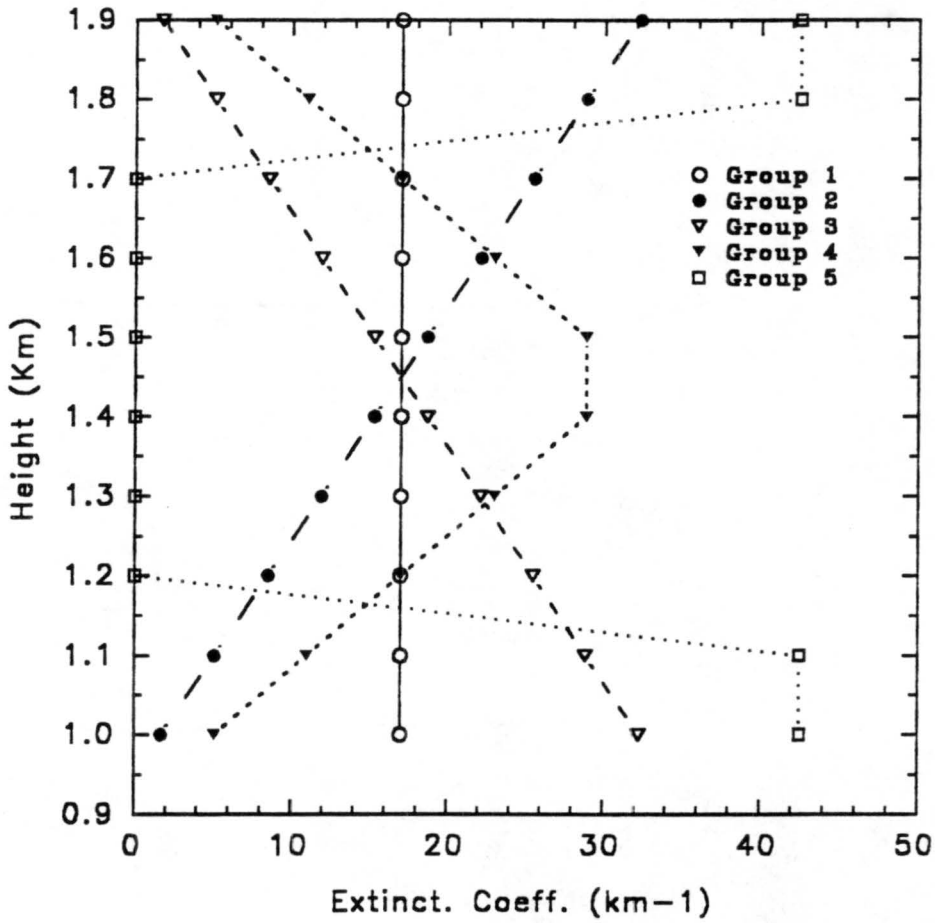

Figure 3.3c. Vertical structure of the extinction coefficient within the cloud for Groups 1a-5a, for the C.1 cloud type.

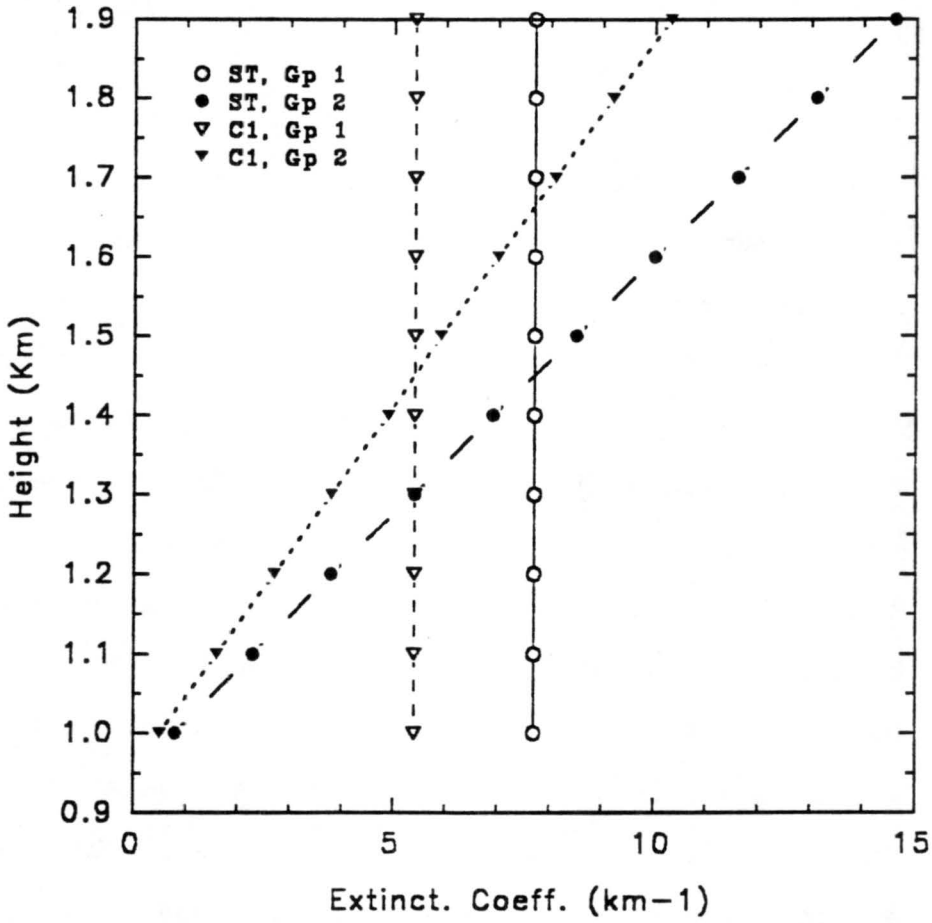

Figure 3.4. Vertical structure of the extinction coefficient within the cloud for Groups 1b and 2b, for ST and C.1 cloud types.

C. Effects of absorption

The atmosphere modeled in this section also contained a single cloud with no background aerosol or Rayleigh interactions. Group 6 clouds had the same structure and input parameters as group 1, the control group, except the single scattering albedo was decreased to 0.99. This cloud structure was modeled after each control group. The single scattering albedo was further decreased to 0.80 to simulate an extremely highly absorbing cloud in group 7.

D. Effects of the subcloud layer

The effects of Rayleigh and background aerosols within the modeled atmosphere was studied. Rayleigh and background aerosol scattering were included within all layers of the modeled atmosphere, and both scattering and absorption by those constituents were considered. An extinction coefficient was computed for the amount of Rayleigh and aerosol scattering to occur within each layer, based on Elterman's (1968) measurements at the wavelength of 0.90 μm. The phase function for background aerosol scatters was approximated by the single scattering phase function for Haze L. Group 8 was equivalent to the control group but contained the addition of Rayleigh and aerosol interactions throughout the modeled atmosphere. Group 9 clouds had an increasing extinction within the cloud and Rayleigh and background aerosol interactions were included in the modeled atmosphere. The group 10 atmosphere was the same as group

9, except the single scattering albedo was decreased from 1.00 to 0.99. Because the amount of aerosol scattering is highly variable (Elterman, 1968), Group 11 was developed to determine the effect of changes in the atmospheric aerosol concentration. Group 11 contained a background aerosol 5 times the standard, and the background aerosol concentration was increased to 10 times the standard in group 12.

E. Effects of precipitation

Precipitation input parameters were based on an assumed monomodal droplet size distribution. Phase function and extinction coefficients were computed in a separate program based on a specific liquid water content, determined from data obtained during the ASTEX program, and constant drop radius. Droplet radius was chosen to be 100 microns. The normalized phase function for rain is depicted in Figure 3.5. Group 13 had a constant extinction within the cloud, liquid water content within the cloud was reduced to 1/3 of the normal, and Rayleigh and background aerosol interactions were considered. Group 14 was identical to group 13 except the single scattering albedo for all interactions was reduced from 1.00 to 0.99. Cloud and rain were the only scattering media allowed in Group 15, and the single scattering albedo was changed to 1.00.

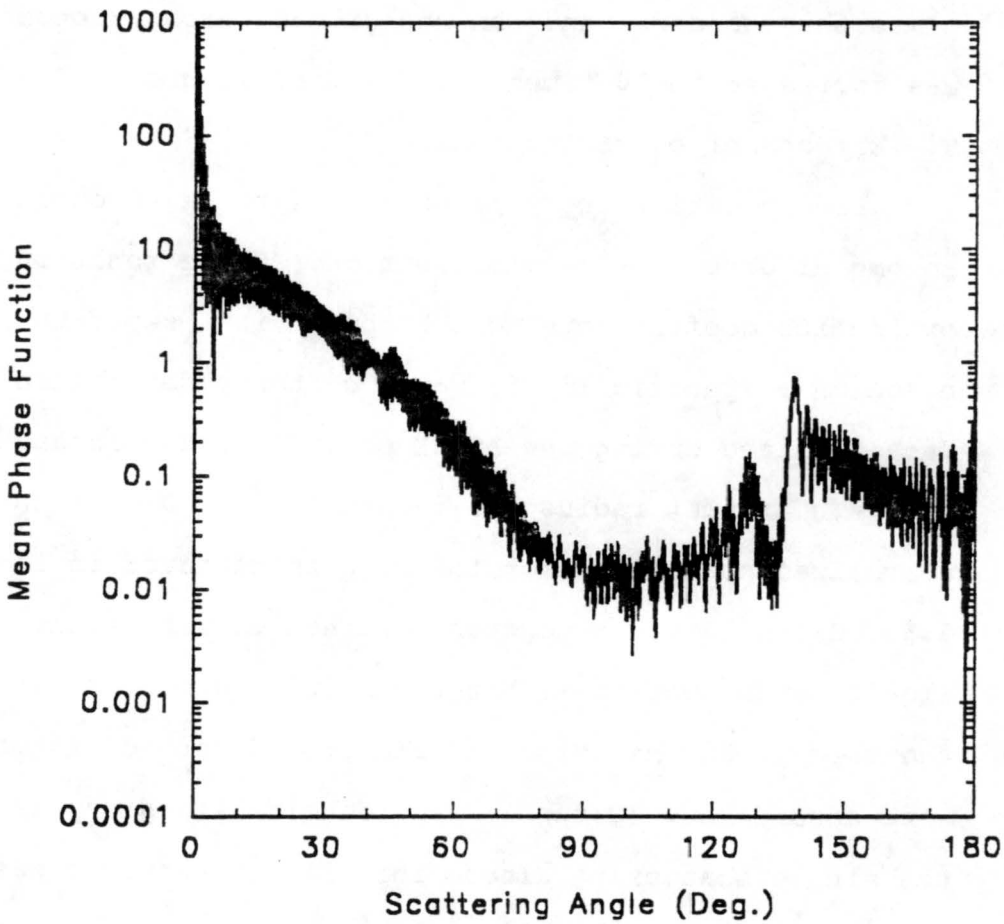

Figure 3.5. Phase function, $P(\theta)$, as a function fo scattering angle, for rain. A constant droplet radius was assumed to be 100 μm.

CHAPTER 4. ANALYSIS OF PHYSICAL PROCESSES

A. General

This chapter presents results produced by the current model. Unless otherwise described, the vertical axis for each graph is the range, or height above the laser ceilometer, in kilometers. The x axis is a measure of the return flux, or probability of returning directly to the ceilometer from the scattering height, as described in Chapter 3. The return flux described here is the sum of the probabilities of returning to the ceilometer for each range gate, for 1 million photons.

To compare the effects of the physical processes modeled, it is convenient to define a nondimensional parameter, α. This factor is determined by

$$\alpha = \frac{C \frac{d\beta_s}{dz}}{\int_0^z \beta_e(z)\, dz}$$

where C is a scaling or normalization factor, with units of km^3. This makes α inversely proportional to the range, z, and to the optical depth, and is a measure of the magnitude of the differential return signal. Within the following sections, α is computed at 10 meters above the cloud base.

For layers that contain no extinction coefficient (a modeling artificiality), an extinction value of $1x10^{-4}$ km^{-1} was assigned to those layers when computing the optical depth. A small value was required to maintain the integrity of α when comparing atmospheres with and without Rayleigh and background aerosols, and this value is at least an order of magnitude less than the Rayleigh and background aerosol extinction coefficient within the lowest 8 km of the standard atmosphere. For the present work, the scaling factor was computed such that $0 \leq \alpha \leq 1$, where small values of α indicate a small differential signal. For cloud heights equal to or greater than 1 km, and extinction coefficients less than 100 km^{-1}, for the constants described above, this resulted in $C = 1.01x10^{-4}$ km^3.

B. Scattering within the cloud

Results from groups 1a through 5a indicate strong ceilometer returns within the lower portion of the cloud. Figure 4.1 depicts the returned energy versus height for the 3 cloud types of group 1a. Specific atmospheric parameters are provided in Table 3.2. It is apparent that, due to the extremely large extinction coefficient for the NS cloud type, a strong return would be produced for any arrangement of the extinction within the cloud. The α factors for each cloud type were calculated to be 0.99996, 0.99982, and 0.99952 for the NS, ST, and C.1 cloud types, respectively. Figure 4.2 shows a comparison of the return from a cloud

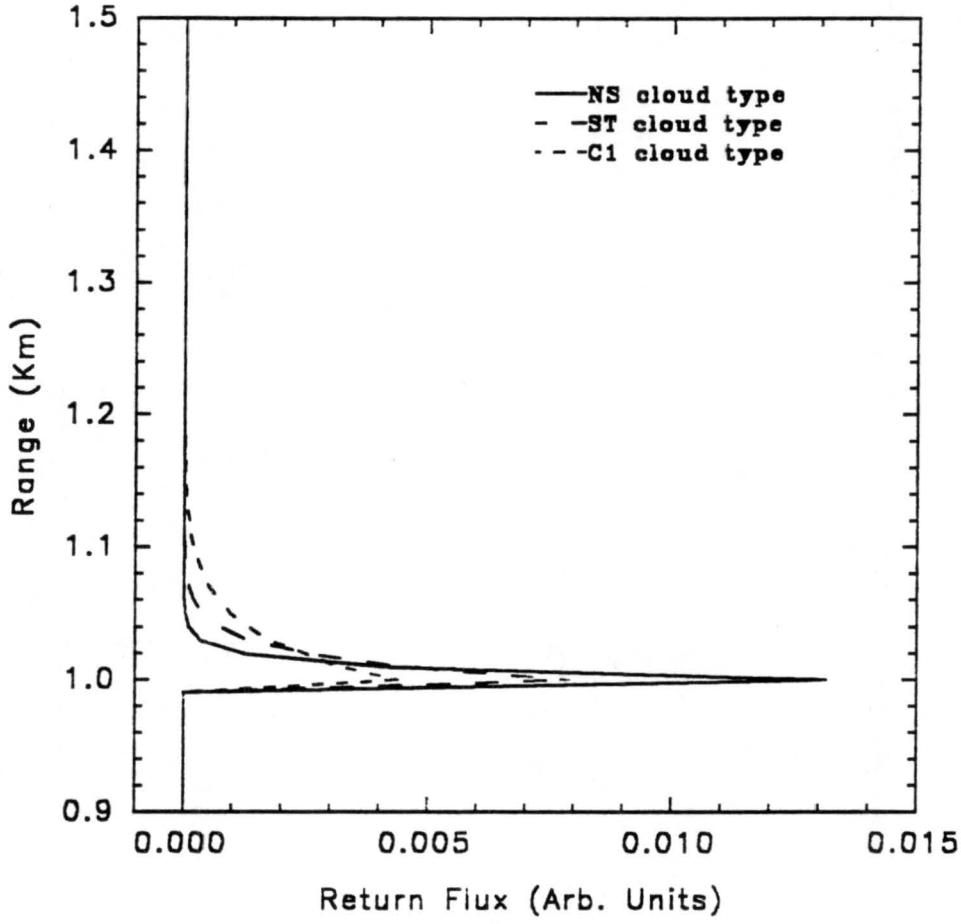

Figure 4.1. Total return flux as a function of range for mean nimbostratus (NS), stratus (ST) and cumulus (C.1) cloud types (Group 1a). The cloud is the only scattering medium within the modeled atmosphere and ω_0 = 1.00 for all three cases.

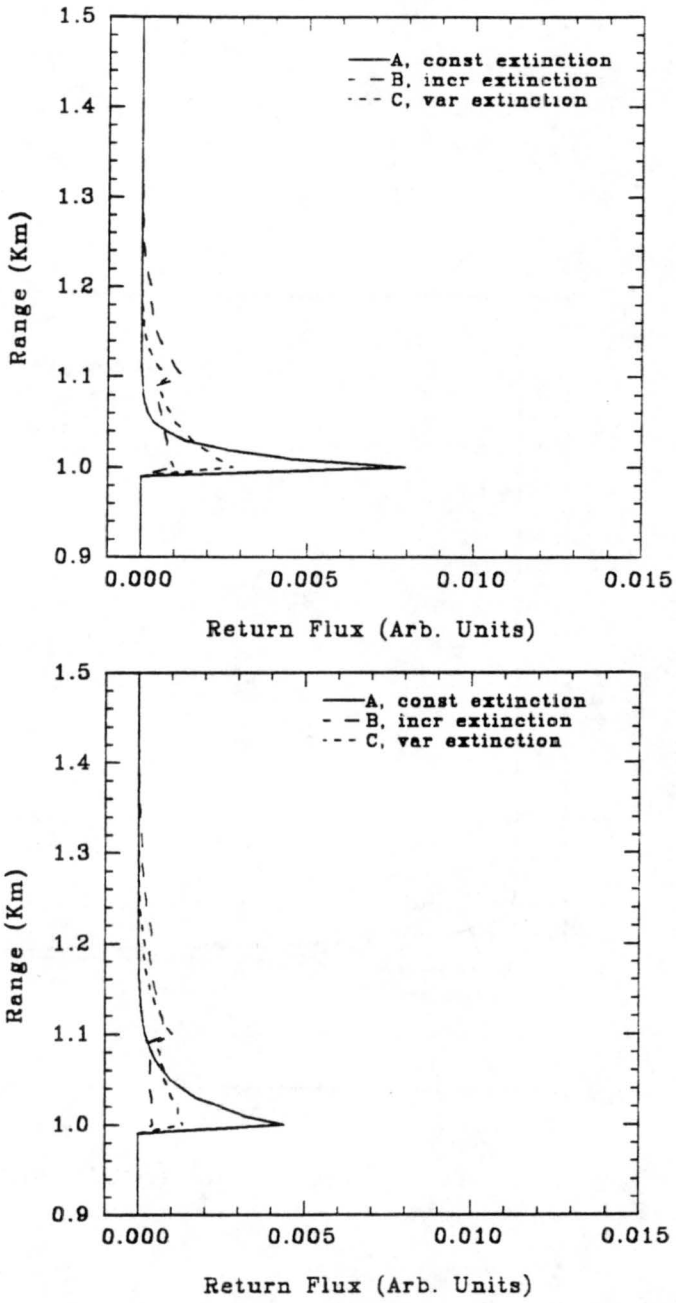

Figure 4.2. Total return flux as a function of range for various profiles of the extinction coefficient within cloud types (a) ST, and (b) C.1. The control group (A=Group 1a) is compared with a cloud having an increasing extinction coefficient with depth (B=Group 2a) and a cloud having the largest extinction within the center of the cloud (C=Group 4a). Optical depth for each cloud is constant.

characterized by a constant extinction through the cloud with the return from a cloud in which the extinction coefficient increases from the cloud base to cloud top. Figure 4.2a presents the ST cloud types of groups 1a, 2a, and 4a (maximum extinction within the cloud center). Figure 4.2b makes the same comparison for cloud C.1. In both cases, group 2a (increasing extinction with cloud depth) produced the weakest returns, but even these model clouds produced a substantial return flux. All of the 1 million photons experienced first order scatters within the lowest 500 meters of the cloud. Group 2a ST type clouds resulted in an α of 0.99725, and the C.1 cloud for this group produced a return of 0.99425. Group 4a α factors were somewhat greater, as expected, due to the larger extinction coefficient near cloud base (ST = 0.99916, C.1 = 0.99814).

Groups 3a and 5a exhibited extremely large extinction coefficients at cloud base and the return flux from very near cloud base was larger than the control groups as a result. Figures 4.3a and 4.3b depict the results from these model clouds for ST and C.1 size distributions and phase functions, respectively. It is evident that these cloud structures would produce a strong return signal for nearly any cloud type of the same depth and optical depth. Values for α for the group 3a cloud types were 0.99995 and 0.99979, and for group 5a, 0.99999 and 0.99987, respectively.

The group b series produced similar results, however,

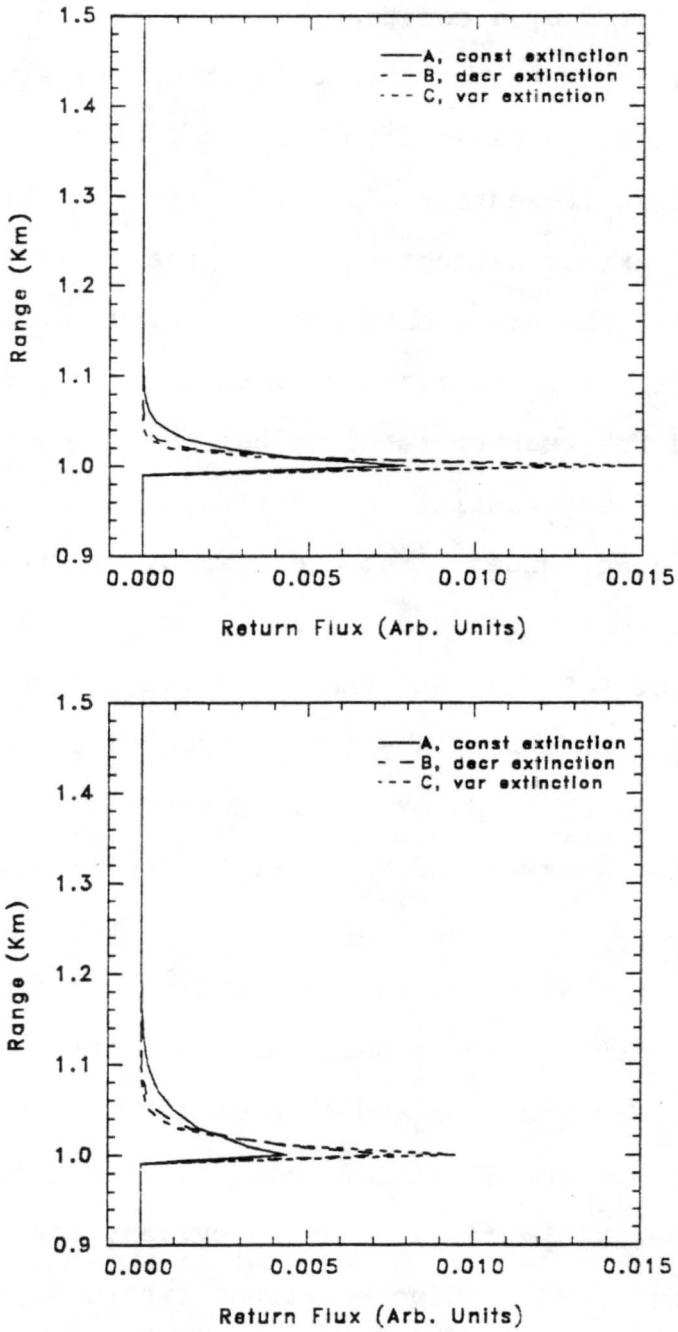

Figure 4.3. Total return flux as a function of range for various profiles of the extinction coefficient within cloud types (a) ST, and (b) C.1. The control group (A=Group 1a) is compared with a cloud having a decreasing extinction coefficient with depth (B=Group 3a) and a cloud having no extinction within the center of the cloud (C=Group 5a). Optical depth for each type is constant.

the magnitude of the returned flux at cloud base and α factors were reduced. Figure 4.4a and 4.4b present results from groups 1a, 1b (ST α = 0.99880, C.1 α = 0.99825) and 2b (ST α = 0.98776, C.1 α = 0.98049) for the ST and C.1 cloud types, respectively. Overall, the photons penetrated much deeper into the cloud before scattering. The clouds containing the increasing extinction coefficients with depth produced a somewhat flatter return than those with constant extinction, however, as Figure 4.5 demonstrates, the cloud base in these models continued to produce a significant return compared to the sub cloud layer. The model runs simulating a decreasing extinction with depth into the cloud and a hole in the center of the cloud once again produced a very strong return at cloud base as a result of the large extinction coefficients associated with the lowest cloud layer. In order to determine how the magnitude of the extinction coefficient within the cloud affected the magnitude of the return, an additional run was made, with the extinction within the cloud 2/3 of the control, group 1a. Figure 4.6 presents the results of the 2 controls and this additional run. These results demonstrate that the magnitude of the return signal is linearly dependent upon the magnitude of the extinction. Figure 4.7 presents the returned energy from first order scatters versus the returned energy from all orders of scattering for the two control groups for cloud type ST. The difference between

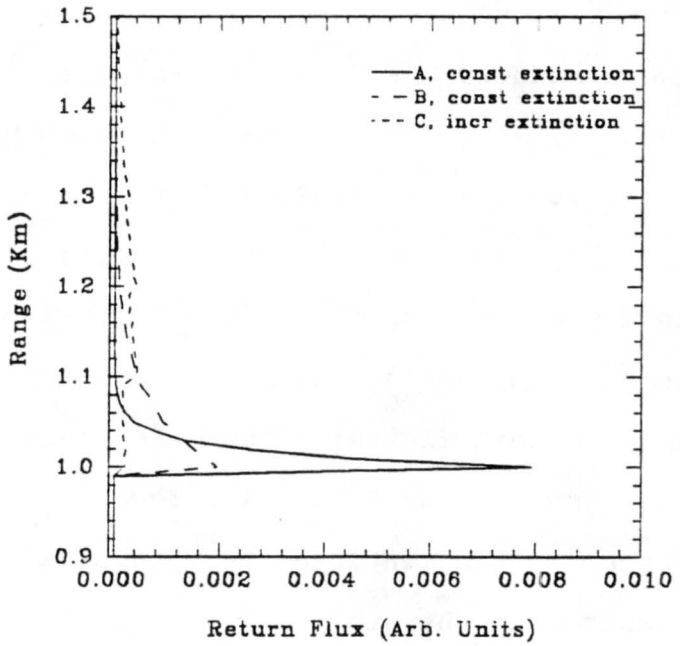

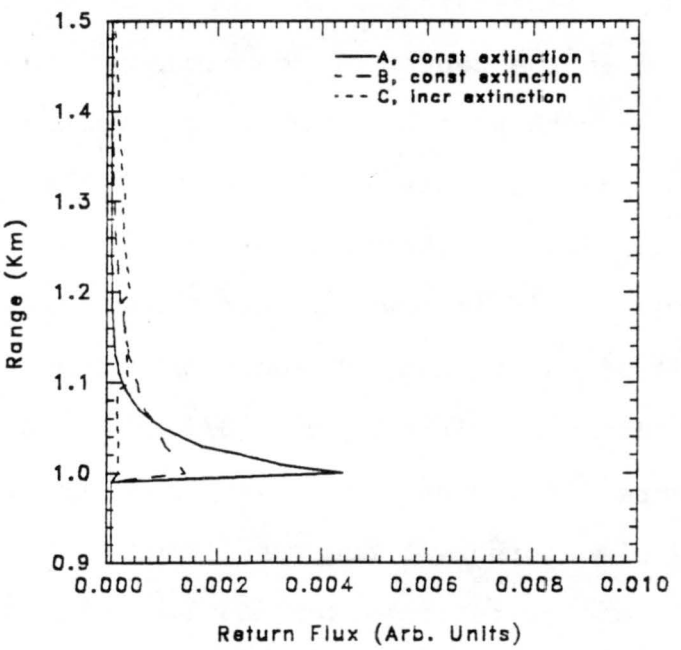

Figure 4.4. Total return flux as a function of range for various profiles of the extinction coefficient within cloud types (a) ST, and (b) C.1. The control group (A=Group 1a) is compared with the second control (B=Group 1b) having one-third the total optical depth, and a cloud with an increasing extinction coefficient with depth (C=Group 2b) but the same optical depth as B.

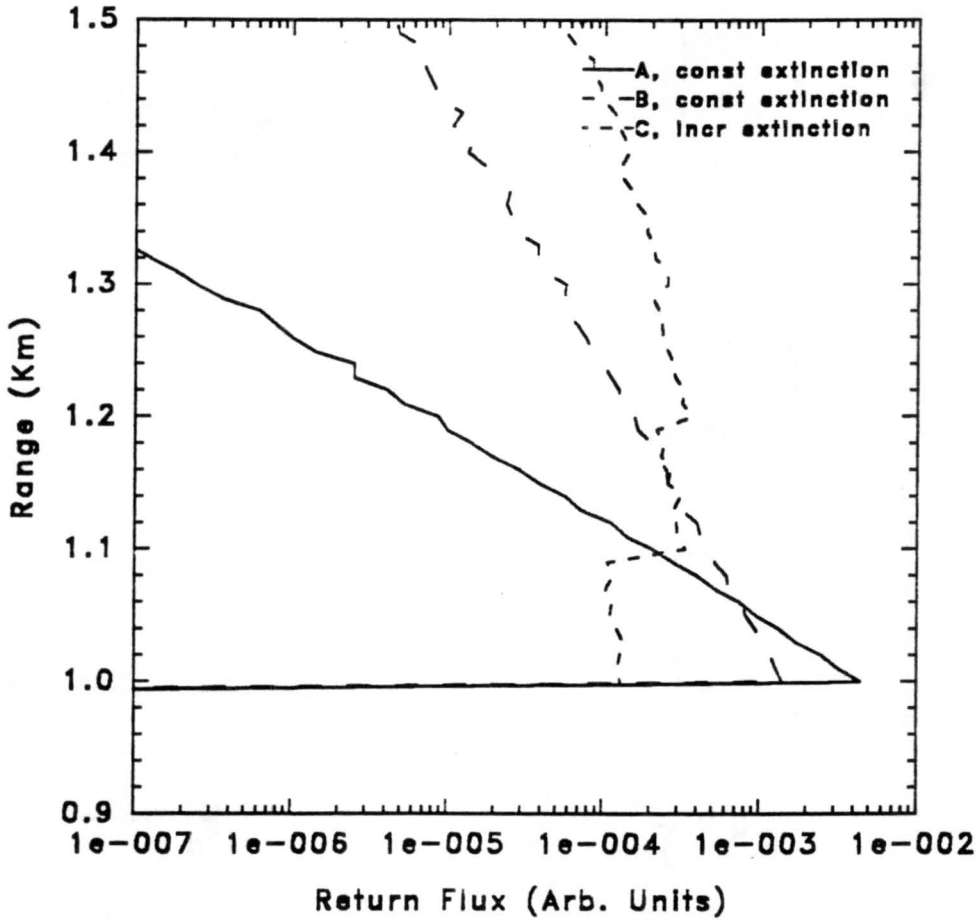

Figure 4.5. Same as figure 4.4(b), but on a logarithmic scale.

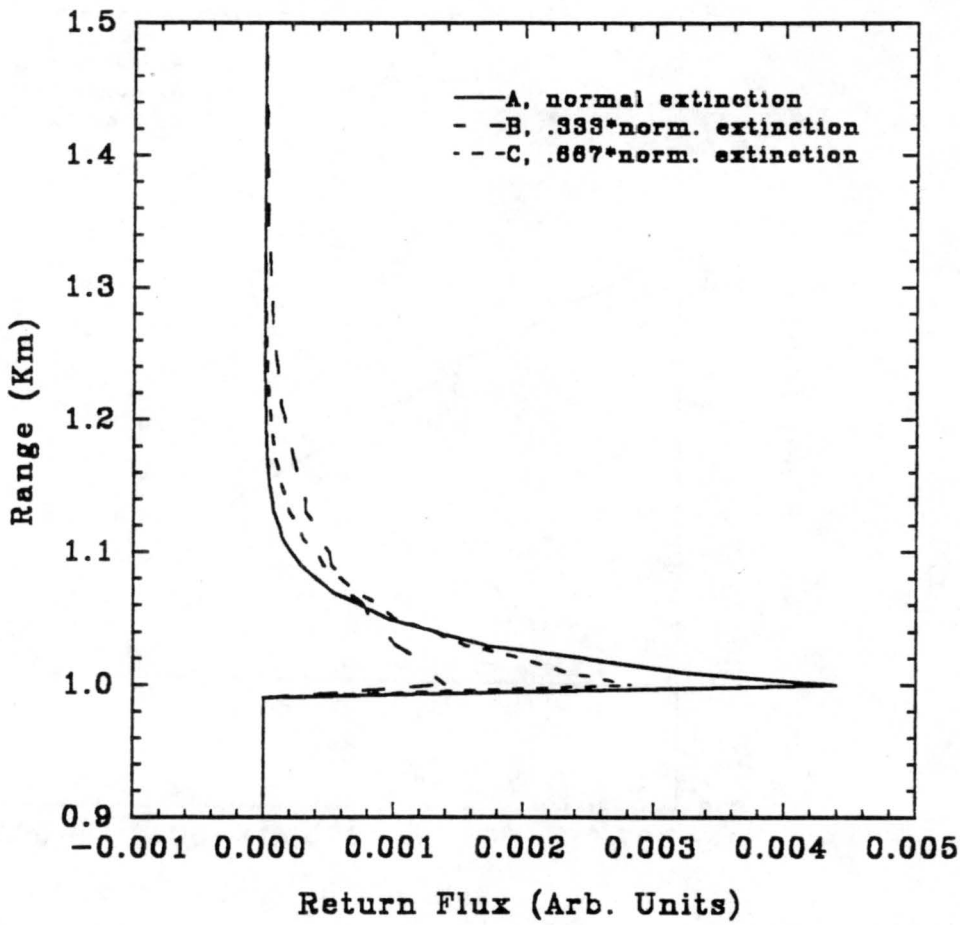

Figure 4.6. Return flux as a function of range for the control groups (A=Group 1a; B=Group 1b) and for a cloud with an extinction coefficient that is 2/3 that for group 1a, for cloud type C.1.

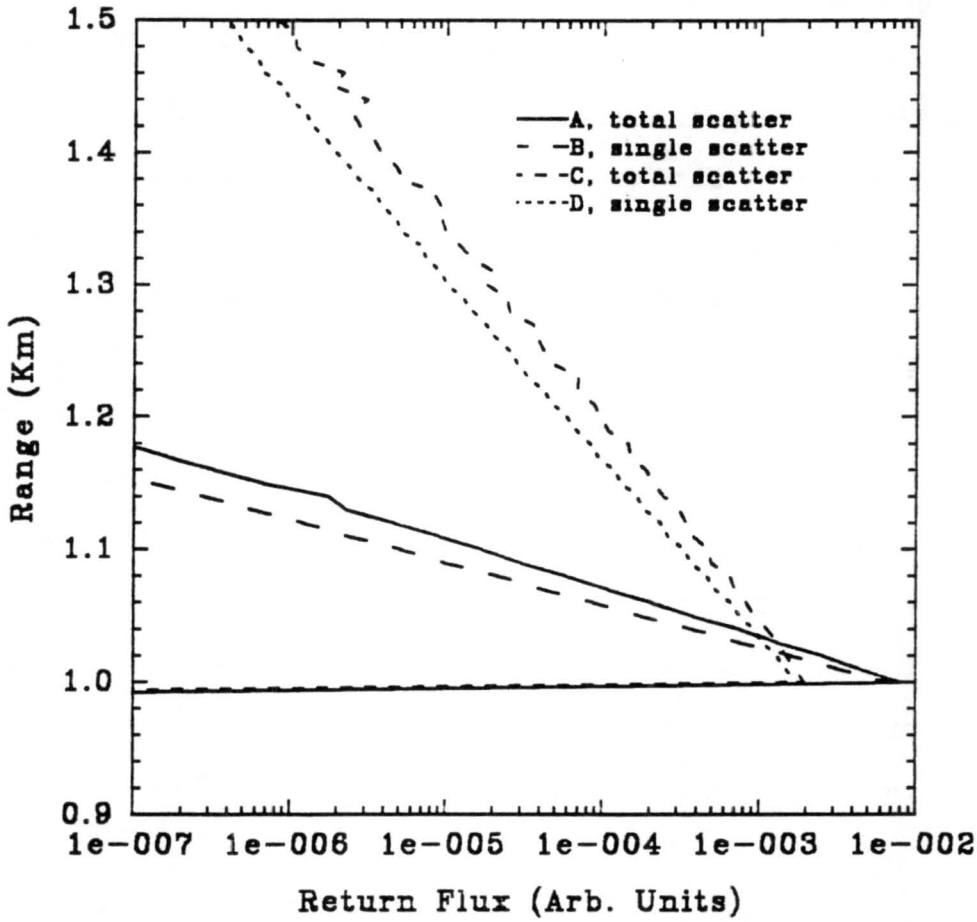

Figure 4.7. Return flux as a function of range and order of scattering for the control groups (A, B=Group 1a; C, D=Group 1b) for cloud type ST.

the two lines represents the increasing contribution by second and higher orders of scattering with depth into the cloud.

The data presented demonstrate that cloud structure can produce large fluctuations in the magnitude and shape of the return signal of the modeled laser ceilometer. For a constant optical depth, the modeled clouds with an increasing extinction with depth produced a weaker and flatter return signal than the clouds with a constant extinction coefficient. Similarly, those with a decreasing extinction produced a stronger, sharper peaked return signal, as a result of the large magnitude extinction coefficients within the lower layers of the cloud. These returns are reflected in the α's computed for these cloud types. The magnitude of the return signal is a linear function of the extinction coefficient. Lastly, higher orders of scattering become more important to the overall returned energy, with increasing depth into the cloud.

C. Absorption

Calculations for the phase functions, extinction information and single scattering albedos were made using a separate program (MIECODE, Eric A. Smith, Dept of Atmospheric Science, CSU, Fort Collins, CO). The program calculated, for λ = 0.90 μm, the actual single scattering albedos for the ST cloud type to be ω_0 = 0.9999517 and for the C.1 cloud type to be ω_0 = 0.9999526, so that absorption

at this wavelength for these cloud types is very small compared to scattering.

Group 6 tested the effect that absorption within the atmosphere has on the overall returned flux of the laser energy. The control groups were based on no absorption within the modeled atmosphere, the single scattering albedo was 1.00. In group 6, the single scattering albedo was reduced to 0.99 for all scatters that occurred. The probability of returning to the receiver, from each scattering point was appropriately reduced by that amount. A comparison of these results with those of the control runs convincingly showed that absorption within the cloud at the level prescribed does not significantly affect the returned flux. For group 6b, the α factors were only slightly reduced from the control, to 0.98882 for the ST cloud type, and to 0.98827 for the C.1 cloud type. The single scattering albedo was further reduced to 0.80 in group 7. Results from this group are displayed in Figures 4.8a and 4.8b, for ST and C.1, respectively, and demonstrate that a highly absorbing cloud will cause a corresponding decrease in the return signal from the cloud. Values for α were 0.79904 and 0.79861, respectively.

The computed single scattering albedo for the modeled clouds at 0.90 μm is generally not less than 0.99. Results produced from the groups described in this section indicate that absorption does not significantly affect the returned

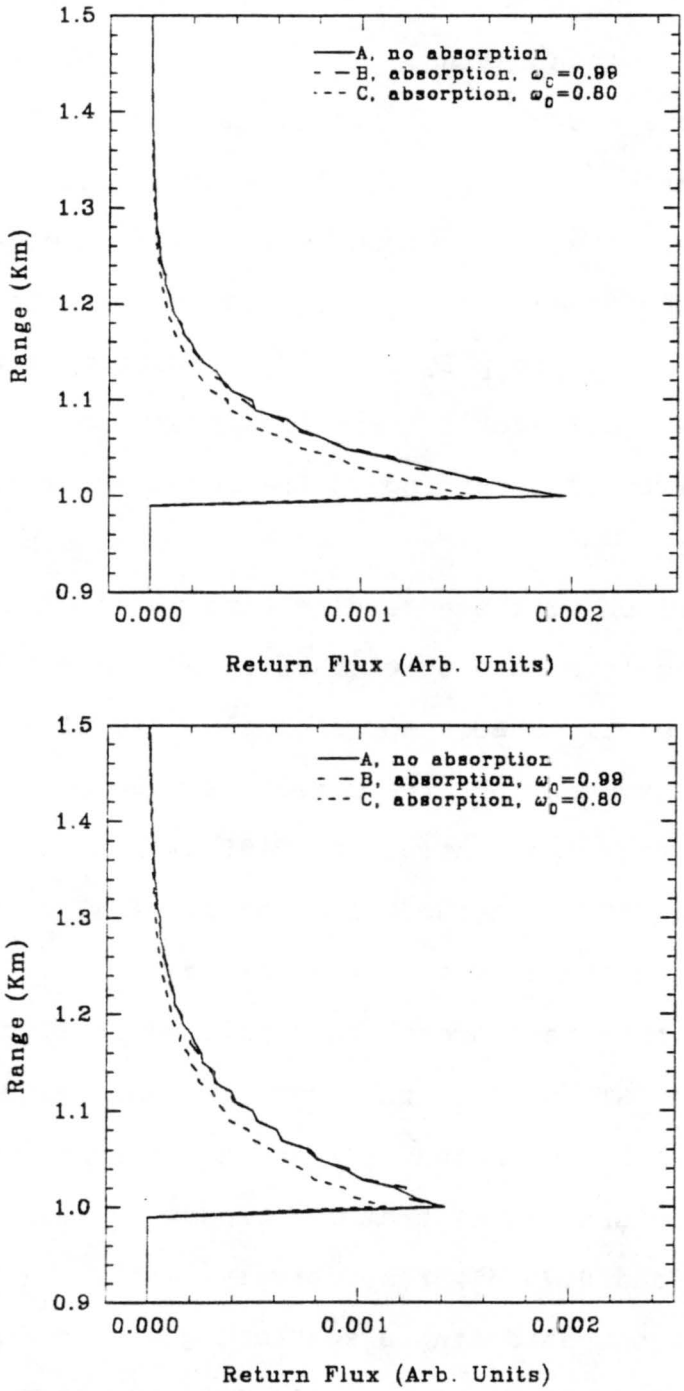

Figure 4.8. Total return flux as a function of range for cloud types (a) ST, and (b) C.1. The control group (A=Group 1b) is compared with clouds that allowed for absorption (B=Group 6b, C=Group 7b) with each scatter.

flux, except in extreme, highly absorbing conditions. In these cases, the returned energy at cloud base may be reduced by as much as 20 percent of the nonabsorbing case.

D. Effects of sub cloud layer extinction

Groups 8, 9, 10, and 11 were developed to determine how Rayleigh and background aerosol interactions affected the ceilometer returns. Extinction coefficients for these parameters were computed within the program and based on data published by Eltermann, 1968. The single scattering phase function for background aerosol scatters was approximated by the phase function for Haze L, and was depicted in a previous chapter.

Figure 4.9 presents 3 group b model runs: (a) the control, (b) the control with the addition of Rayleigh and background aerosol scattering within the modeled atmosphere (Group 8b), and (c) the parameters described in (b) above, with the addition of absorption (ω_0 = 0.99) for all interactions (Group 10b). As in the previous section, absorption did not significantly affect the results. The addition of Rayleigh and background aerosol interactions, however, significantly altered the simulated ceilometer returns. Because of the inverse square dependence on the range, the return flux was largest within the first few range gates, and it decreased rapidly up to cloud base, even though relatively few photons scattered within this part of the atmosphere. This decrease in the differential return

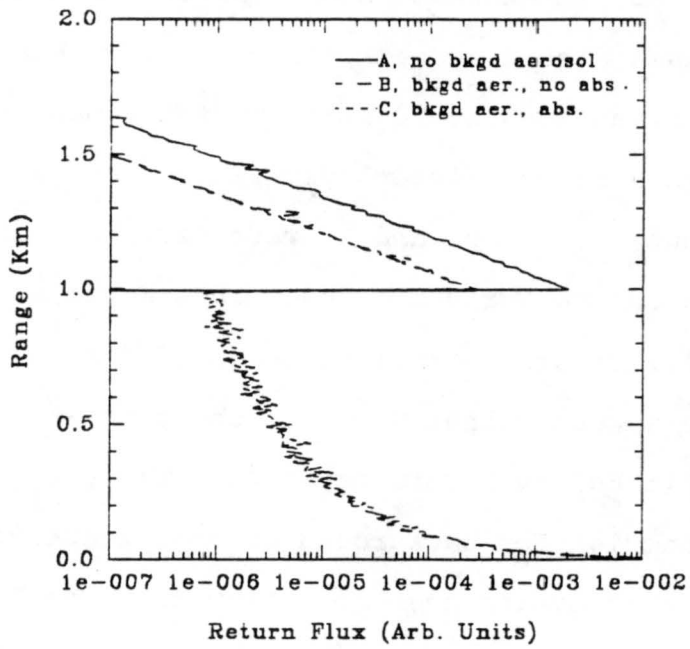

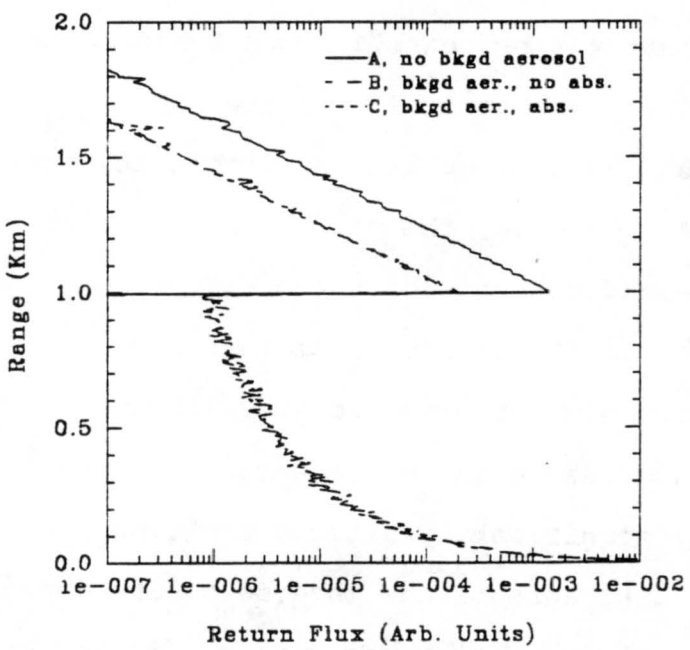

Figure 4.9. Total return flux as a function of range for cloud types (a) ST, and (b) C.1, and various atmospheric profiles. The control group (A=Group 1b) is compared with an atmosphere containing Rayleigh and background aerosol scattering, with no absorption (B=Group 8b) and with absorption (C=Group 10b).

signal was reflected in α factors that dropped to 0.38834 and 0.30755 for the ST and C.1 cloud types. For the modeled atmosphere, the magnitude of the returned flux below approximately 200 meters was larger than the return from the cloud. Figure 4.10 depicts similar results for clouds with an increasing extinction coefficient (Groups 2b and 9b) with cloud depth. Values for α for the ST cloud type decreased from 0.98776 in group 2b to 0.058947 in group 9b. The values for α for the C.1 cloud types lowered similarly.

Within the atmosphere, the number and size distributions of aerosols vary greatly, and the phase function is strongly dependent on particle size. The Haze L phase function used for the background aerosol may not be appropriate as a result. In addition, the variation in number density causes changes in the extinction coefficient for the background aerosol. The standard background aerosol extinction was increased by a factor of 5 for Group 11. Figure 4.11 presents the results based on this increase, and also for a tenfold increase (Group 12) in the background aerosol. Both cases portray a significantly decreased signal from the cloud. Group 11 values for α were 9.47×10^{-3} and 4.57×10^{-3} for the ST and C.1 cloud types. The values for α decreased to 2.92×10^{-3} and 4.39×10^{-4} for group 12.

The overall effect of the addition of Rayleigh and background aerosol interactions on the return signal is to decrease the difference between the return signal just below

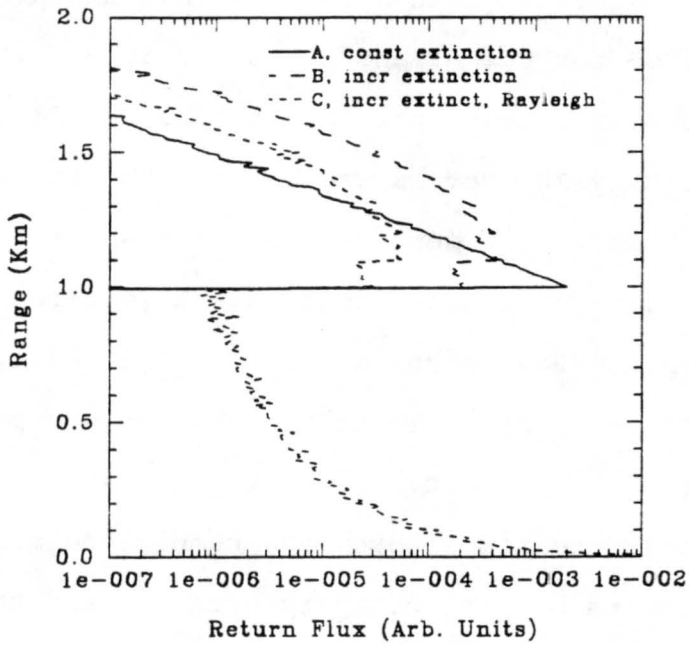

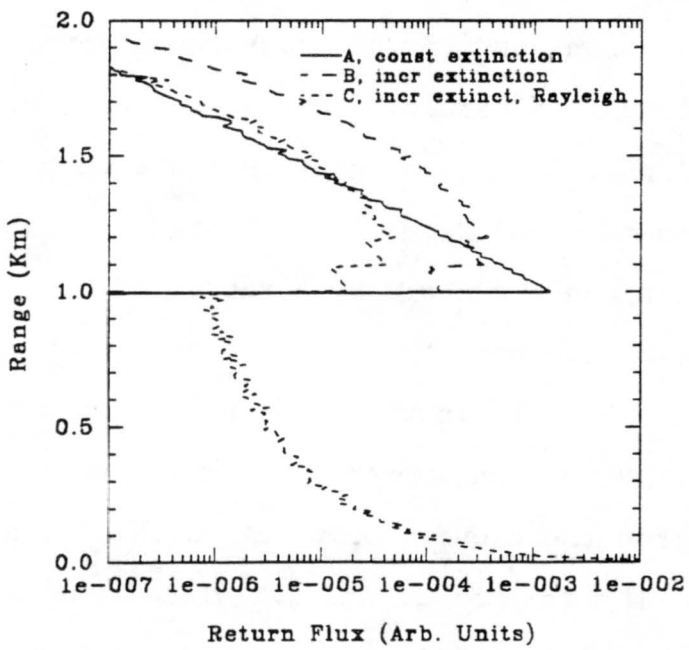

Figure 4.10. Total return flux as a function of range for cloud types (a) ST, and (b) C.1, and various atmospheric profiles. The control group (A=Group 1b) is compared with a cloud containing an increasing extinction coefficient with depth (B=Group 2b), and with B with the addition of Rayleigh and background aerosol scattering (C=Group 9b).

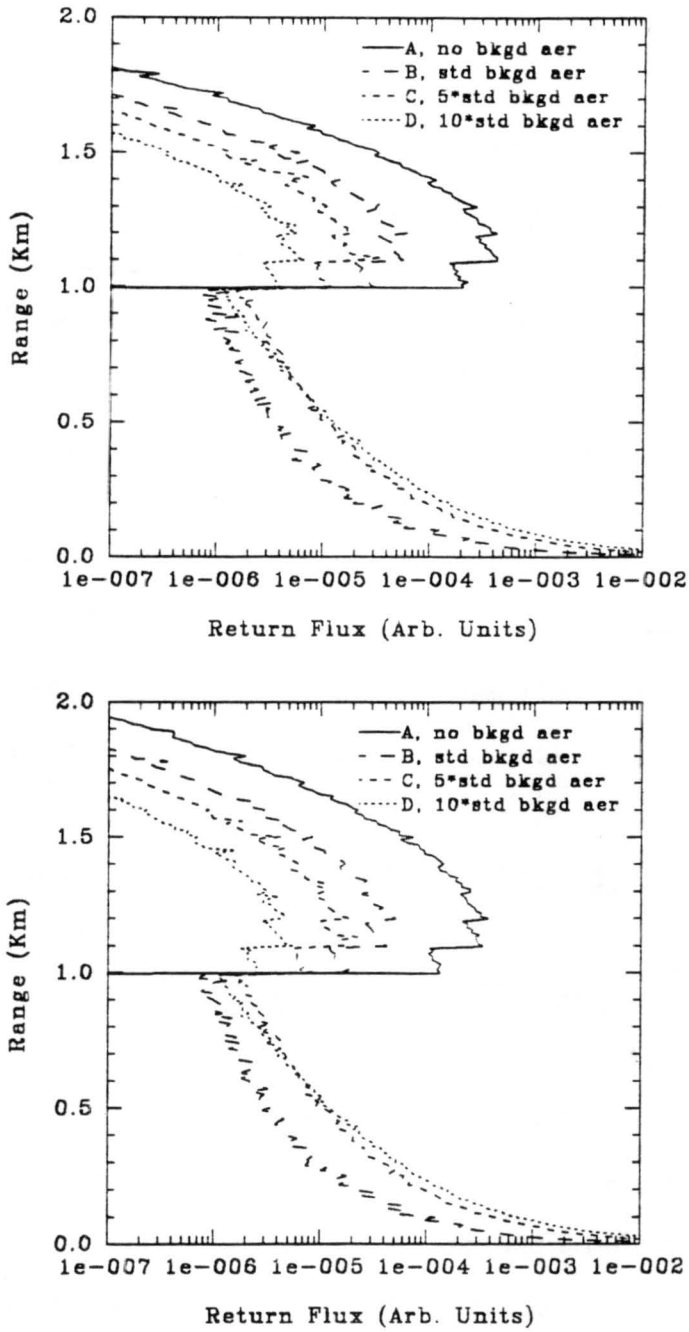

Figure 4.11. Total return flux as a function of range for cloud types (a) ST, and (b) C.1, and various atmospheric profiles. The control group (A=Group 2b) is compared with a cloud containing an increasing extinction coefficient with depth (B=Group 9b), and with B with the addition of Rayleigh and background aerosol scattering (C=Group 11b, D=Group 12b).

cloud base and the signal within the lower portions of the cloud. This is accomplished in two ways. First, the signal below the cloud layer is increased as result of scatters that occur within that layer. The introduction of these additional particles within the model atmosphere also decreases the probability that a photon scattered within the cloud will reach the detector, by increasing the extinction from the scattering point within the cloud, to the ceilometer receiver.

E. Precipitation effects

Several groups were produced to determine how rain affected the ceilometer return. A monomodal drop size distribution was assumed, and the rain was inserted homogeneously in the layer from the cloud base to the surface. Standard Rayleigh and background aerosol extinctions, clouds, and rain comprised Group 13. Group 14 included absorption (ω_0 = 0.99) for all interactions, and Group 15 was composed of the cloud and rain only. Figure 4.12 presents the control, group 13, and group 14. Once again, there was no significant difference between the absorbing and nonabsorbing cases. An interesting shift in the magnitude of the return signal occurred between the Rayleigh and background aerosol case and the case with Rayleigh, background aerosol, and rain interactions. The rain caused an increase in the return signal throughout the subcloud layer, but a large decrease in the return signal

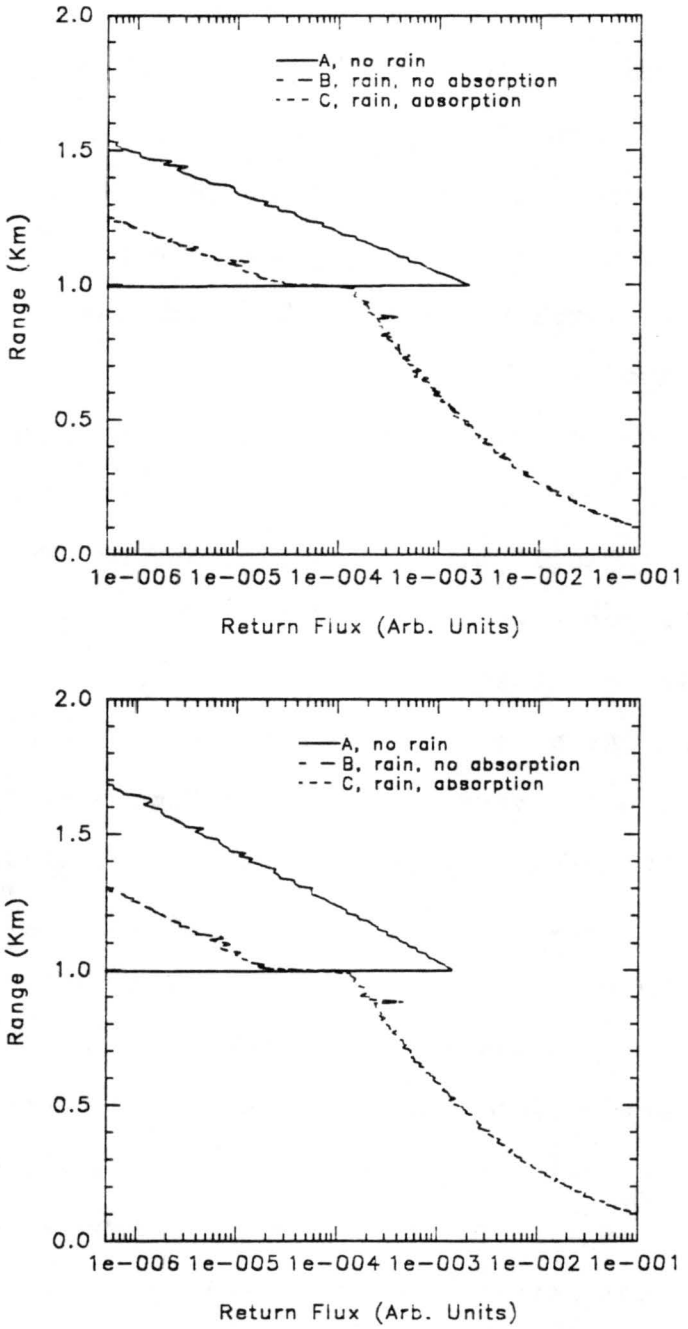

Figure 4.12. Total return flux as a function of range for cloud types (a) ST, and (b) C.1, and various atmospheric profiles. The control group (A=Group 1b) is compared with the same cloud, with the addition of Rayleigh and background aerosol scattering throughout the atmosphere, and rain below the cloud (B=Group 13b), and with B with the addition of absorption (C=Group 14b).

within the cloud. The increase in the extinction below the cloud, caused by the rain, acted to increase the low altitude return signal. As a result, less energy reached the cloud and, of the energy that did reach the cloud, the energy travelling to the ceilometer had to traverse the high extinction subcloud layer. This decrease in the signal level caused by the rain is further illustrated in Figure 4.13, which depicts group 15, the group containing rain, but no Rayleigh or background aerosols. The rain extinction coefficient is 20 times greater than that for the Rayleigh and background aerosols, and the return signal in the case with rain and background aerosols is dominated by rain scatters. As a result, there is very little difference between the two cases depicted in Figure 4.13. The α factors for group 13b were 0.02418 and 0.01432, and for group 15, 0.02573 and 0.01532. Magnitudes of the α factors predict that the differential return signal should be greater for the group with no Rayleigh and background aerosol extinction, which the results support.

In summary, rain within the subcloud layer will decrease the return signal from the cloud and significantly increase the return from the subcloud layer, due to the relatively large extinction coefficient of the rain. The return signal from the cloud will experience this decrease in magnitude, as a result of the increase in optical thickness within the subcloud layer.

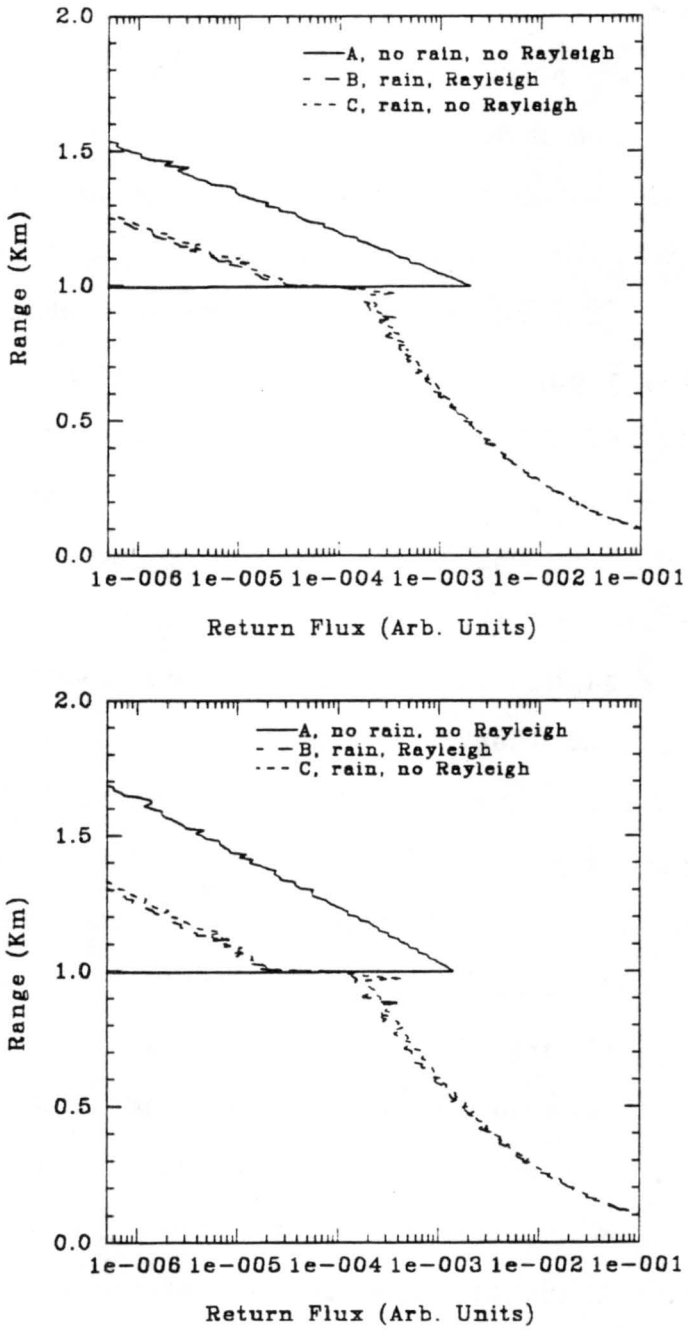

Figure 4.13. Total return flux as a function of range for cloud types (a) ST, and (b) C.1, and various atmospheric profiles. The control group (A=Group 1b) is compared with the same cloud, with the addition of Rayleigh and background aerosol scattering throughout the atmosphere, and rain below the cloud (B=Group 13b), and with B without Rayleigh and background aerosol scattering (C=Group 15b).

F. Detectability Threshold

Since α was computed at a constant range, z, variations in α for these model atmospheres are produced strictly by changes in the optical depth, τ, or by changes in the volume scattering coefficient. As a result, it is possible to graphically depict the model atmospheres where the two variables, τ and $d\beta_s/dz$, represent the abscissa and ordinate, respectively. Figure 4.14 presents the model atmospheres as a function of these two parameters.

Model runs which were created to evaluate the effect of cloud extinction structure on the ceilometer return are denoted in Figure 4.14. Based on the assumptions above, it is possible to identify an area on the figure which generally represents the probable combinations of τ and $d\beta_s/dz$ that describe this physical process. As depicted in the figure, most of this area is characterized by relatively large values of α. The cases developed to test the effect of absorption are also indicated in the figure. Again, an area can be described on the graph that represents probable combinations that define the absorption cases, and most of this area is represented by relatively large values of α. Model runs that were produced to determine the effect that the subcloud layer extinction had on the return signal are depicted in the figure. The area representing this physical process is depicted on the lower portion of the graph, and small values of α are typical for this area.

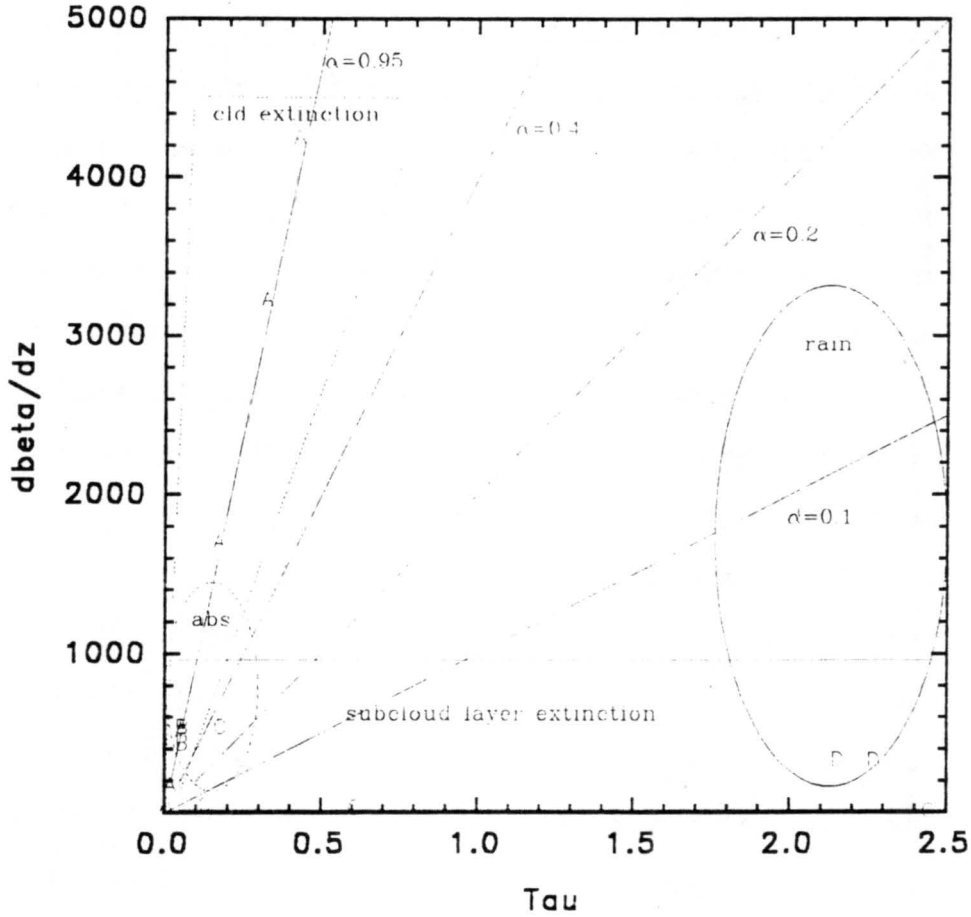

Figure 4.14. Modeled atmospheres as a function of the variables, τ and $d\beta_e/dz$, and general areas representing the modeled physical processes: (1) cloud extinction structure, (2) absorption, (3) subcloud layer extinction, and (4) precipitation. Lines of constant α are also denoted.

Cases for the last physical process tested, rain, are also indicated in the figure, and an area describing probable variations in τ and $d\beta_s/dz$ for this process is described. Small values of α are characteristic of this process also.

A threshold value, α_{min}, may then be defined as the minimum value of α for which clouds are detectable. For the modeled atmospheres described in this chapter, $\alpha_{min} \approx 0.10$, and is depicted in Figure 4.15. This selection of α_{min} is supported by the values of α computed for the model runs, and by the modeled ceilometer return signal signature. Much of the areas identified for subcloud layer extinction and rain fall below the detectability threshold, while those areas representing absorption and cloud extinction structure tend to be well above α_{min}.

A review of the values for α and the differential return signal demonstrates that increases in the background aerosol within the atmosphere, and particularly within the subcloud layer, has the most profound effect upon the differential return signal. A strong flux of aerosols in the intervening atmosphere between the ceilometer and the cloud will significantly reduce the ceilometer return signal from the cloud. The addition of rain within the subcloud layer will also decrease the ceilometer return signal substantially. The structure of extinction within the cloud has less impact, however, within an atmosphere containing Rayleigh and background aerosol extinction, cloud

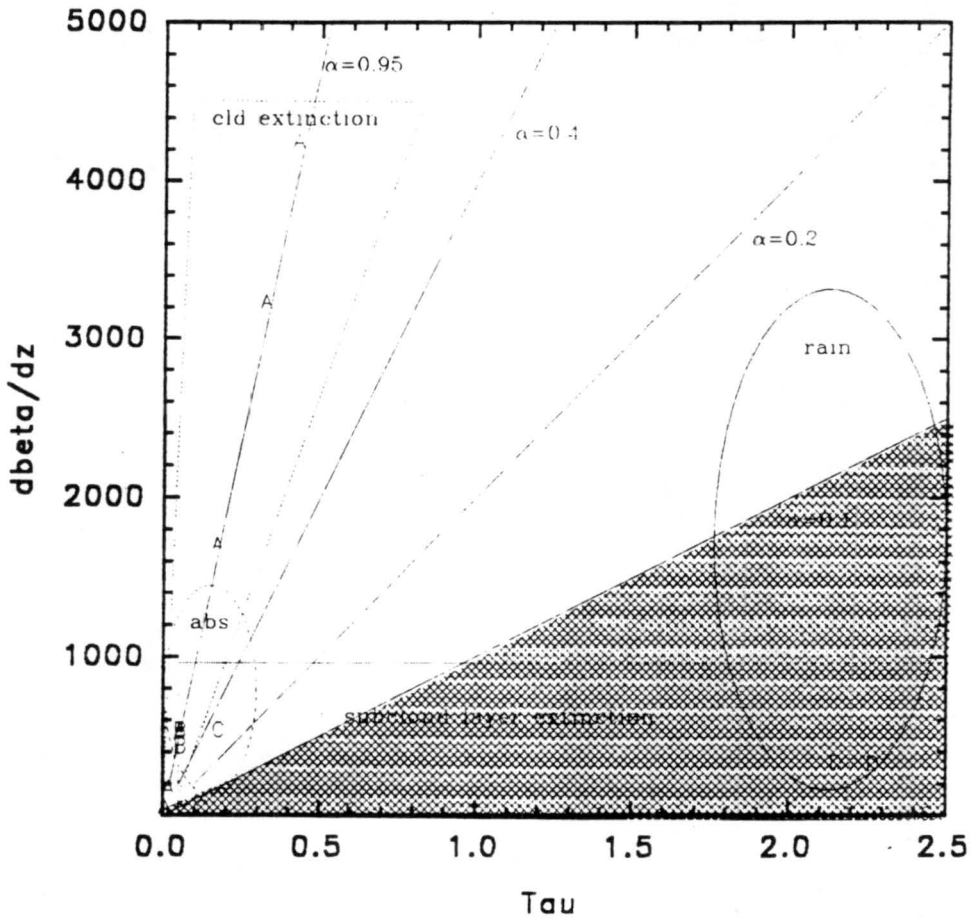

Figure 4.15. Modeled atmospheres as a function of the variables, τ and $d\beta_e/dz$, and general areas representing the modeled physical processes: (1) cloud extinction structure, (2) absorption, (3) subcloud layer extinction, and (4) precipitation. Also denoted are lines of constant α. The shaded region identifies the area below α_{min}.

structure becomes somewhat important. A cloud with an increasing extinction coefficient with depth, which is typical of some newly forming clouds, will cause the differential return signal to decrease. The model results and the values for α demonstrate that absorption within the limits prescribed have the least effect on the differential return signal. A comparison of the computed α factors for the model runs with the selected $\alpha_{min} \sim 0.10$, indicates that rain and variations in the subcloud layer are the likely causes for clouds to not be detected.

CHAPTER 5. ANALYSIS OF THE RETURN SIGNAL

A. General

This chapter describes the application of this model to a few actual measurements obtained during the ASTEX program. The next section describes some of the characteristics of the laser ceilometer used during the experiment, and how these parameters were modeled within the current research. The last section in the chapter briefly compares the modeled ceilometer output to case studies.

B. Modeled ceilometer parameters

The laser ceilometer parameters modeled are those associated with the ceilometer used during the FIRE and ASTEX experiments, and contains a .901 micron wavelength gallium arsenide laser transmitter. The transmitter and diode receiver are located adjacent to each other within the field unit. These are collocated within the model. The height range of the ceilometer is from 15 meters to 7600 meters, and range gates are 7.6 meters apart.

The ceilometer identifies clouds by making a comparison of the return signal difference, rather than using absolute values of the signal. The ceilometer first measures a background noise. In order to compensate for the strong dependence of the return signal on the inverse of the

range squared, a swept gain is introduced in the ceilometer. An oscilloscope was used to determine the gain, and this was normalized to 1.0 within the model. The normalized gain is presented in Figure 5.1. The gain increases sharply for nearly half of the ceilometer range, then levels off, resulting in smaller return fluxes for cloud heights approaching the maximum range of the ceilometer. This effect is illustrated in Figure 5.2, where three modeled clouds are the same in every respect except their heights.

The ceilometer takes a set of readings during the sampling period, firing the laser prior to taking each set of readings. For each set of readings, the measured return, as a function of range, is compared with the background noise for each range bin. An integer value of 1 is given to each range bin that has a measured return greater than the noise, and 0 is assigned for each bin with a return equal to or less than the noise. This is repeated a finite number of times, M (M = 5120). The integers are then summed for each range bin. The value M/2 is subtracted from that sum. An example of the actual ceilometer output is provided in Figure 5.3. An algorithm within the ceilometer then compares the integer return to a threshold value for each range gate. If the magnitude of the integer exceeds that of the value of the threshold for a specific range bin, the ceilometer associates the presence of a cloud within that bin. The height of the lowest such bin is classified as the

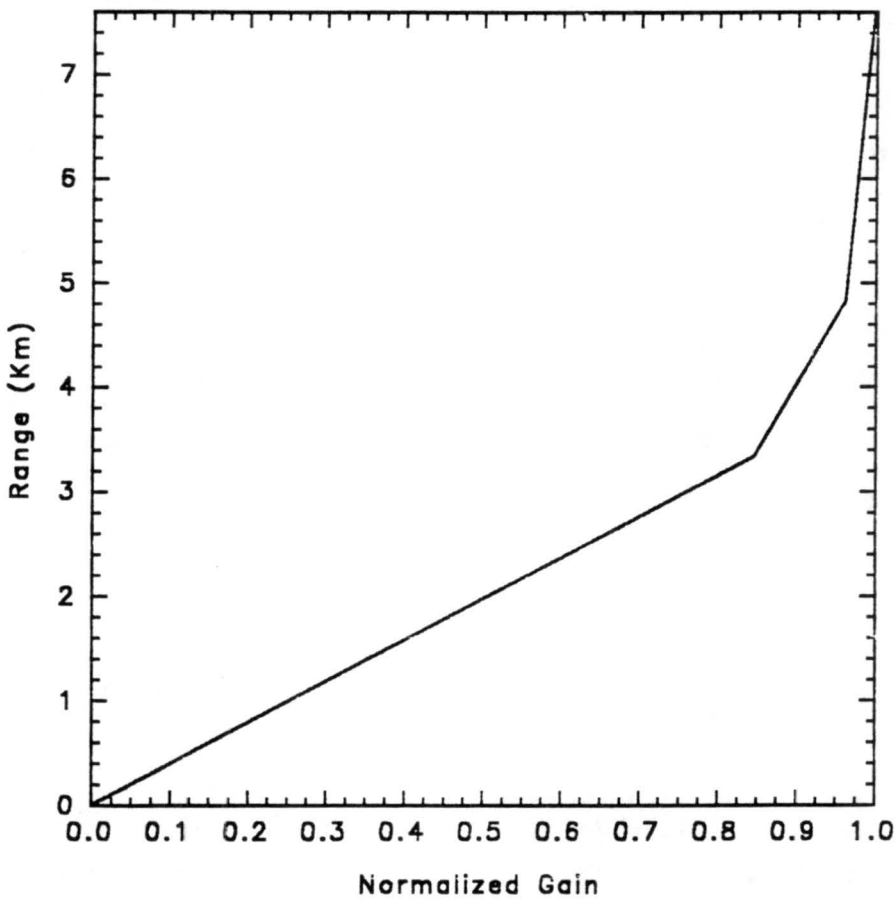

Figure 5.1. Normalized swept gain used within the current model. Gain slope pictured is equal to the gain used by the laser ceilometer used during the FIRE and ASTEX programs.

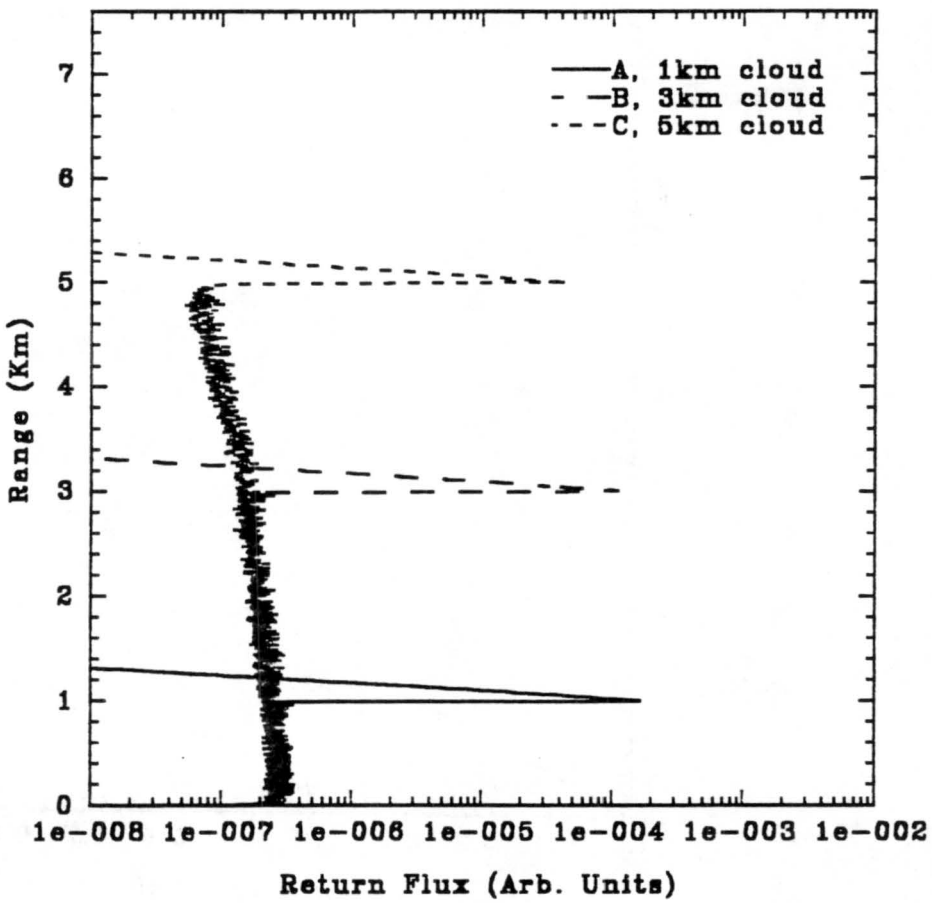

Figure 5.2. Effect of the normalized gain on three similar clouds. The cloud bases are located at (a) 1.0 km, (b) 3.0 km, and (c) 5 km. Phase functions and extinctions used are for cloud type C.1.

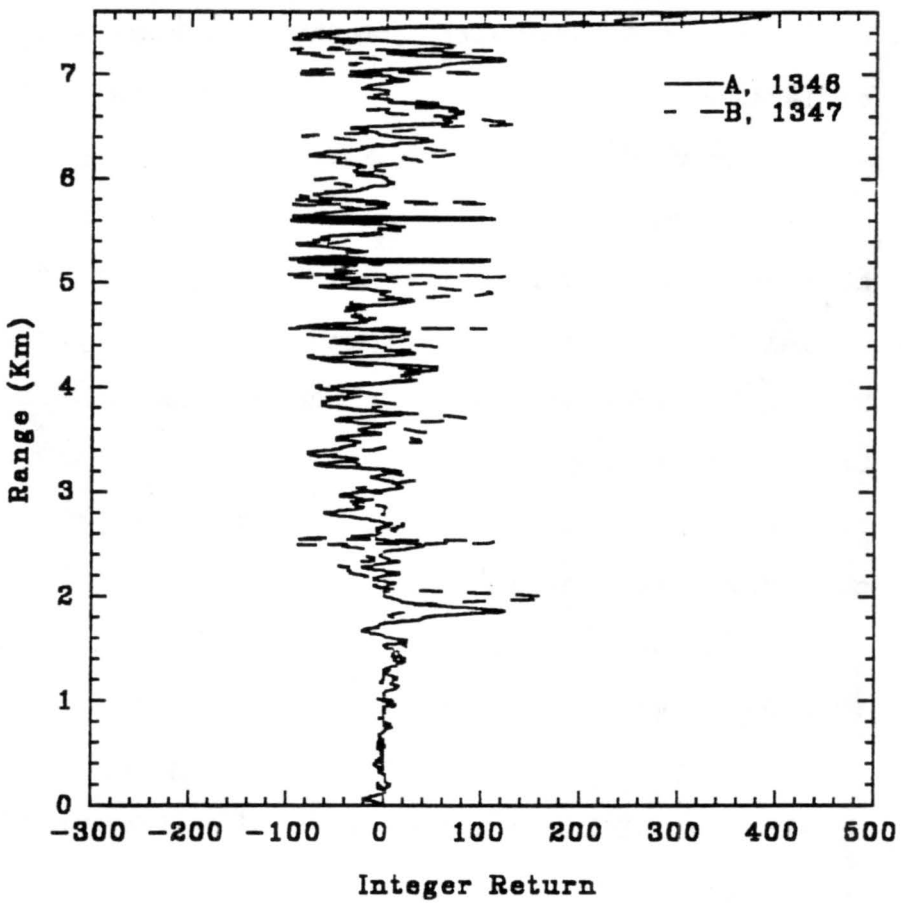

Figure 5.3. Actual laser ceilometer output obtained during the ASTEX program for (a) 07 Jun 92, 1346 GMT and (b) same date, 1347 GMT.

cloud base height. Additional parameters are included within the ceilometer algorithm, but are not modeled at this time.

Elterman (1968) demonstrated that background aerosol extinction may vary as much as an order of magnitude within the first 10 km above the earth's surface, and these variations can be even larger near terrain features. If a symmetric variation in the extinction about the mean is assumed, then this variation in the background aerosol can be inferred. Figure 5.4 presents the return flux for Rayleigh and average background aerosol extinction, and for Rayleigh with the five times the published average background aerosol extinction, for a clear sky condition. The return flux depicted has been adjusted by the normalized gain described earlier.

As in chapter 4, α is a measure of the differential return signal, and can be used to develop a model of the methodology of the ceilometer described above. The addition of the normalized gain to the model converted the model output to a more linear function. As a result, clouds within the current model may also be identified by the magnitude of the return signal difference. The detectability threshold, α_{min}, as introduced in chapter 4, can be determined based on the laser ceilometer and atmospheric variables. This value is a function of the background noise and the range. A value of α less than α_{min}

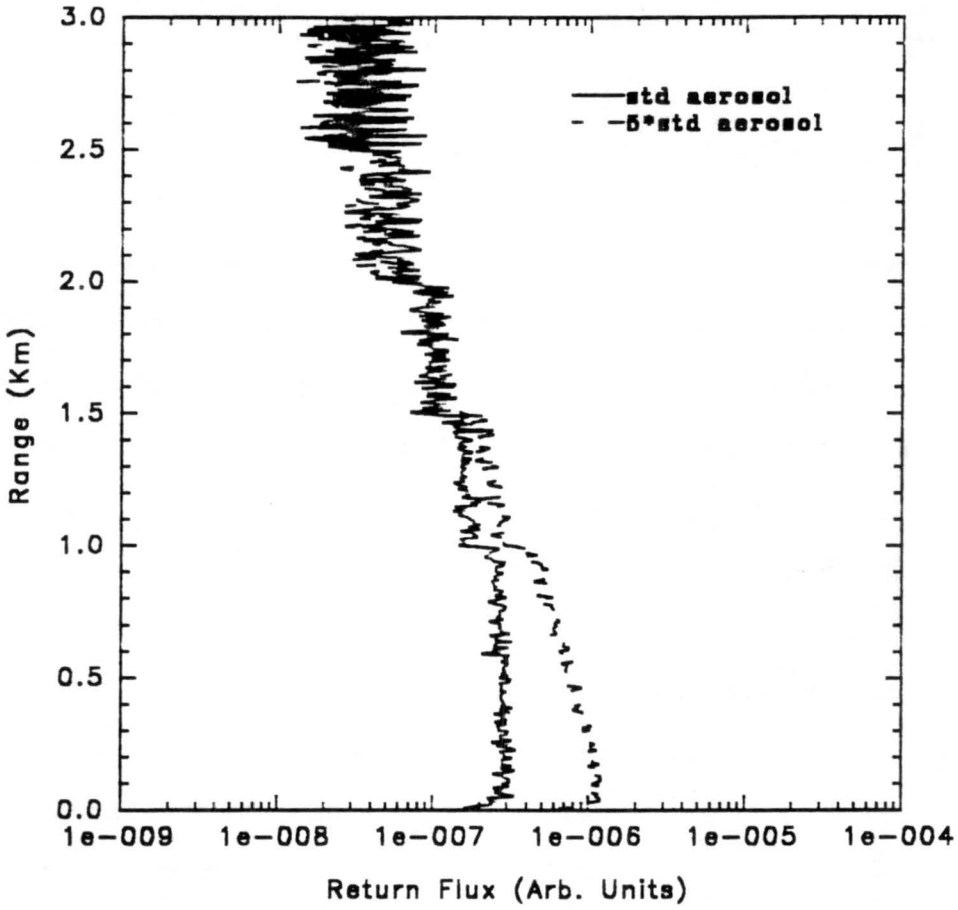

Figure 5.4. Modeled return flux for Rayleigh and background aerosol only. Represented are (a) Rayleigh with standard background aerosol extinction, and (b) Rayleigh with five times standard background aerosol extinction.

results in the model ceilometer identifying no cloud at that height. The sum of α_{min} and the background noise acts as the threshold parameter within the ceilometer algorithm, and would have to be great enough to overcome fluctuations in the background aerosol content and noise combined, to prevent these variations from being mistakenly identified as a cloud.

C. Atmospheric media

An atmosphere containing standard aerosol concentrations, Rayleigh scattering, and a cloud at 4 km was modeled. The cloud contained a liquid water content consistent with that found in similar clouds that were somewhat lower in altitude during the ASTEX program. Results from the experiment are depicted in Figure 5.5, which shows that the cloud is easily identified from the return signal. An α was computed for a depth of 7.6 meters within the cloud, and was found to be equal to 0.0929.

The model was reinitialized with several changes in the modeled atmosphere. The background aerosol content within the atmosphere was increased to 5 times the standard concentration, within the limits prescribed by Elterman (1968). Since liquid water content and as a result, extinction coefficient vary with temperature, the extinction of the modeled cloud at 4 km would be somewhat lower than that found in the low clouds during ASTEX. The extinction coefficient was decreased to one-half of the

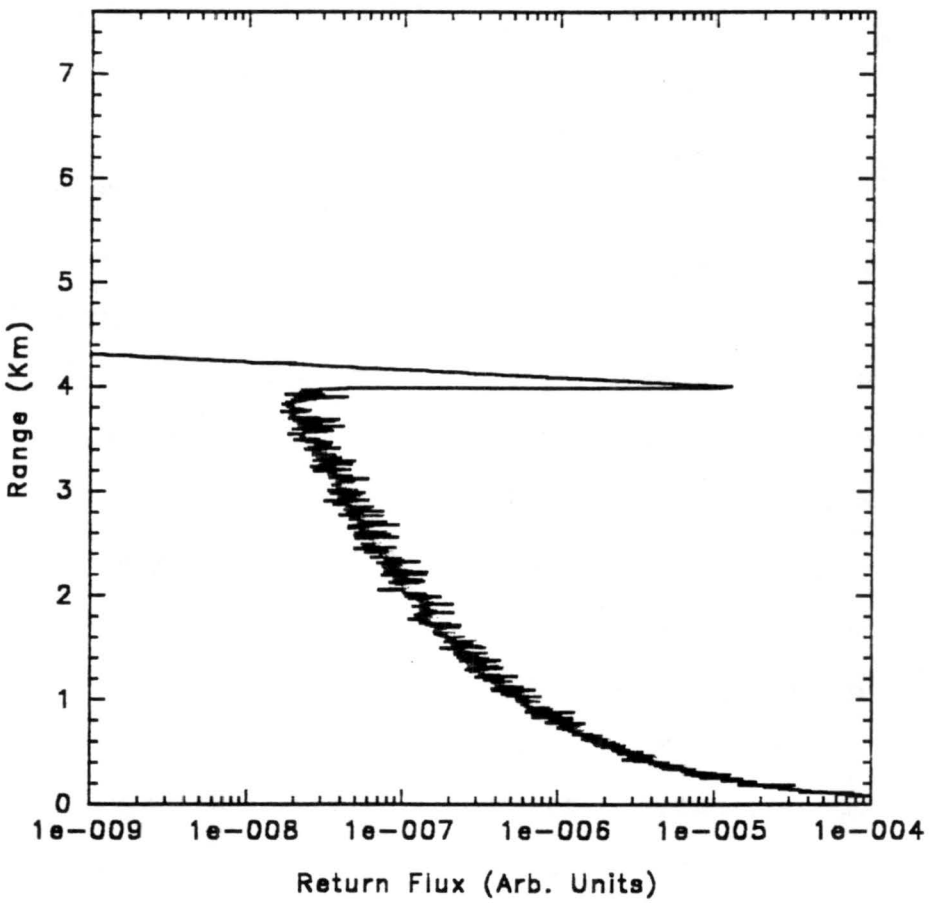

Figure 5.5. Return flux for a representative cloud. Cloud base height is 4 km, and Rayleigh and background aerosol are distributed throughout the modeled atmosphere.

original extinction. Figure 5.6 presents the results produced by the model for these atmospheric conditions. The α factor computed for this run was 0.0108. To determine the minimum value for α, α_{min}, it is necessary to consider the maximum expected variation in the background aerosol concentration. An order of magnitude variation of the background aerosol concentration at 4 km results in a computed α of 7.3×10^{-3}. Assuming the background noise, including reflected solar energy and system noise, produces an equivalent α that is only half of the amount produced by the background aerosol, α_{min} at 4 km would be equal to 0.0110, greater than that produced by the cloud. Using the modeled cloud and the assumptions presented, the ceilometer would not recognize the signal return as a cloud. Figure 5.7 presents the return signal for a similar cloud at 6 km. In this case, $\alpha = 0.044$. The computed $\alpha_{min} = 4.81 \times 10^{-3}$, based on an equivalent background noise used above. For this atmosphere with 5 times the background aerosol and one-half the extinction (assuming the cloud is composed of liquid water), $\alpha = 4.68 \times 10^{-3}$, again insufficient to be identified as a cloud by the ceilometer.

In summary, the parameter, α_{min}, was used as the detectability threshold with which to identify clouds within the modeled ceilometer. The results indicate that atmospheric conditions could exist such that the modeled ceilometer may not be capable of identifying some clouds.

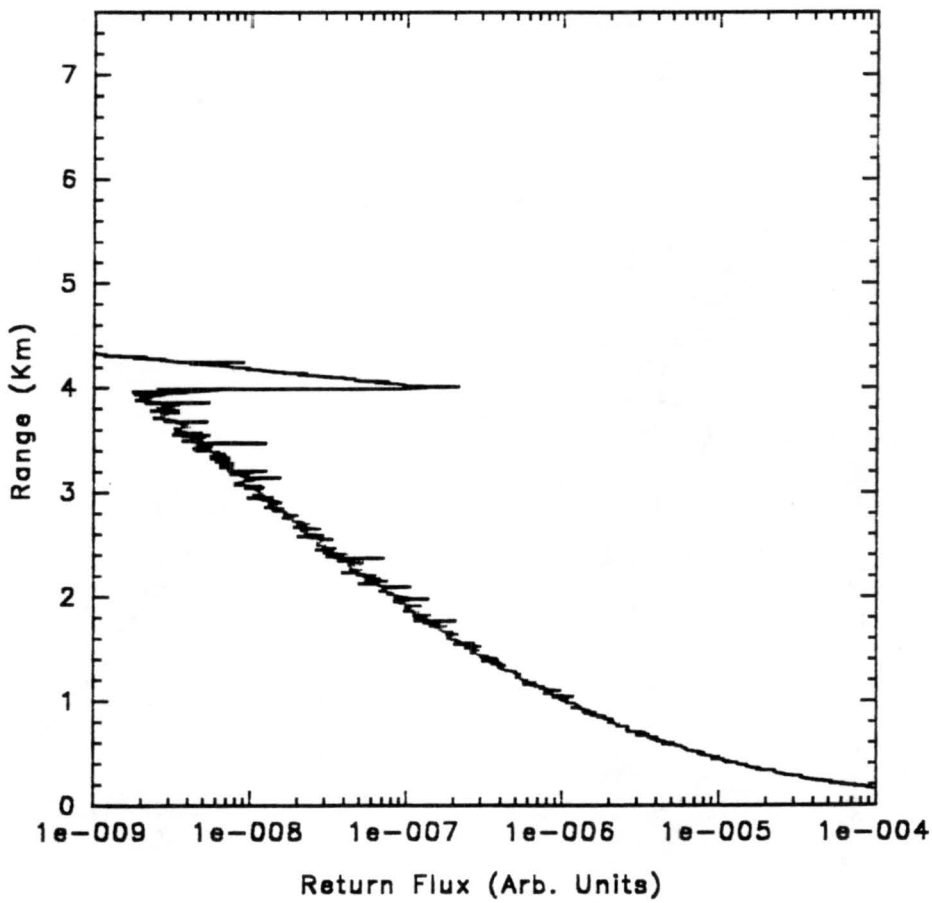

Figure 5.6. Return flux for an atmosphere containing five times the standard concentration of background aerosol. Cloud base height is 4 km, and extinction coefficient for the cloud is 0.5 that in Figure 5.5.

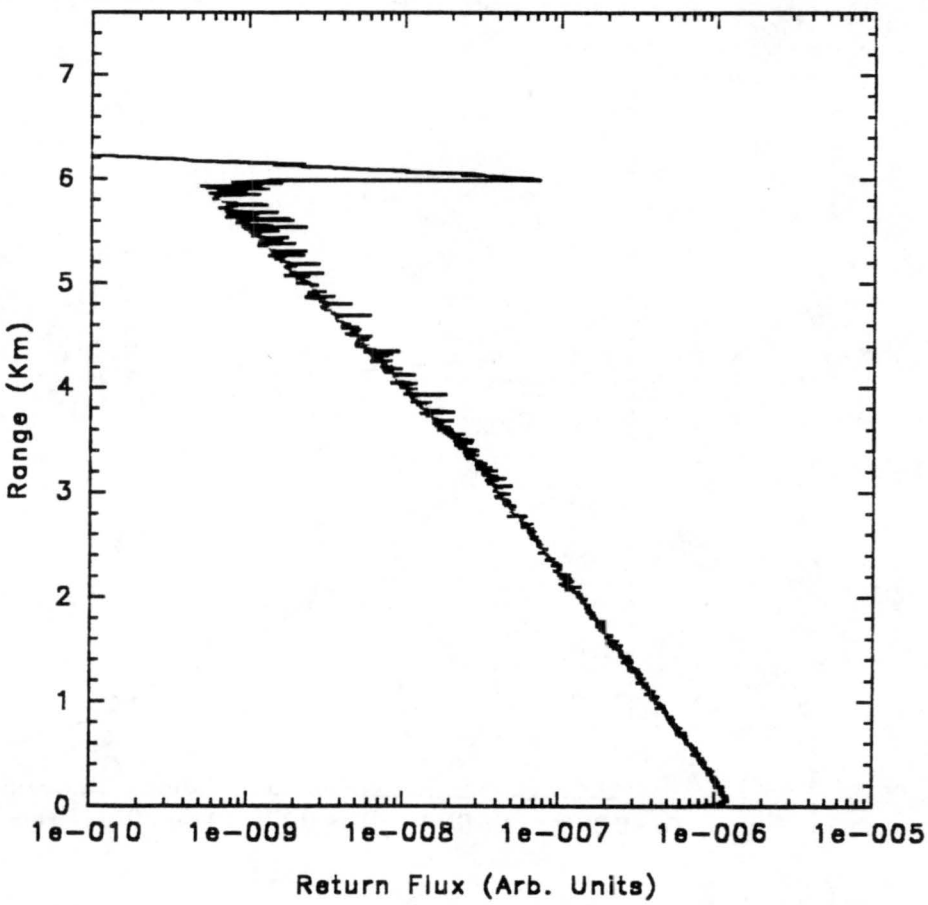

Figure 5.7. Return flux for a cloud near the maximum range of the laser ceilometer used during the ASTEX program. Cloud base height is 6 km, and Rayleigh and background aerosol are distributed throughout the modeled atmosphere.

CHAPTER 6. CONCLUSIONS

Initial analysis of the data from the ceilometer used during the FIRE and ASTEX programs indicated that clouds were sometimes not reported even though clouds were visible over the ceilometer. In order to understand this inconsistency, a model using Monte Carlo techniques has been refined to study the effect that multiple scattering has on the performance of the near infrared (0.90 micron wavelength) gallium arsenide laser ceilometer used during those programs.

Output from the current Monte Carlo model was compared to the results from Plass and Kattawar (1971), Kunkel (1974), and Eloranta (1972), and show reasonable agreement with all of the previous studies.

Specific parameters within the atmosphere were then modeled in order to understand the effect that each had on the signal return. Atmospheric variables modeled included the cloud extinction profile, cloud extinction magnitude, absorption, the subcloud layer extinction profile, and the presence of rain. The parameter, α, was defined to allow for quantitative comparisons of the effects that each parameter had on the amount of change in the ceilometer return signal, and was defined so that it was inversely

proportional to the range and the optical depth. The parameter, α, was defined as

$$\alpha = \frac{C\frac{d\beta_s}{dz}}{\int_0^z \beta_e(z)\,dz}.$$

Cloud structure can produce large fluctuations in the magnitude and shape of the return signal of the modeled laser ceilometer. For a constant optical depth, the modeled clouds with an increasing extinction with depth produced a weaker and flatter return signal than the clouds with a constant extinction coefficient. Similarly, those with a decreasing extinction with depth produced a stronger, more sharply peaked return signal, as a result of the large magnitude of the extinction coefficients within the lower layers of the cloud. The magnitude of the return signal near cloud base is a linear function of the extinction coefficient. The model results also demonstrated that higher orders of scattering become more important to the overall returned energy, with increasing depth into the cloud.

Two sets of runs were made to determine how absorption affected the ceilometer return signal. The first set contained a single scattering albedo of 0.99, the single scattering albedo was further reduced to 0.80 in the second set. A comparison of these results with those of the

control runs convincingly showed that absorption within the cloud at the level prescribed does not significantly affect the returned flux, except for highly absorbing situations. A highly absorbing cloud caused a corresponding decrease in the return signal from the cloud.

The addition of Rayleigh and background aerosols within the modeled atmosphere was also studied. The overall effect of the addition of Rayleigh and background aerosol interactions on the return signal was to decrease the difference between the return signal just below cloud base and the signal within the lower portions of the cloud. This behavior has two interrelated sources. First, the signal from below the cloud layer was increased as result of the increased extinction within that layer; this also results in a lower level of radiation incident on the cloud base. Second, the introduction of these additional particles within the model atmosphere decreased the probability that a photon scattered within the cloud will reach the detector, by increasing the attenuation from the scattering point within the cloud, to the ceilometer receiver.

The fourth parameter introduced in the model was rain. A monomodal drop size distribution was assumed. Rain within the subcloud layer will decrease the return signal from the cloud and significantly increase the return from the subcloud layer, due to the relatively large extinction coefficient of the rain. The return signal from the cloud

also experienced a decrease in magnitude, as a result of the increase in the attenuation within the subcloud layer.

The corresponding values for α for each of the physical processes above demonstrate that an increase in the background aerosol within the atmosphere, and particularly within the subcloud layer, has the most profound effect upon the differential return signal. A high concentration of aerosols in the intervening atmosphere between the ceilometer and the cloud will significantly reduce the differential return signal from the cloud. The addition of rain within the subcloud layer will also decrease the differential return signal substantially. The cloud structure has less impact; however, within an atmosphere containing Rayleigh and background aerosol extinction, cloud structure does become important in a secondary sense. A cloud with an increasing extinction coefficient with depth, which is typical of some newly forming clouds, will cause the differential return signal to decrease. The model results and the values for α demonstrate that absorption within the limits prescribed have the least effect on the differential return signal.

A detectability threshold, α_{min}, was defined. Based on results from the modeled atmospheres, the value of $\alpha_{min} = 0.10$ was assigned. A graphical depiction of the physical processes modeled as functions of the optical depth and $d\beta_s/dz$ indicated that the inability to detect clouds is most

likely due to variations in the subcloud layer extinction or the addition of rain, and is least likely due to cloud extinction structure and absorption.

Data reduction procedures specific to the ceilometer used in the ASTEX program were incorporated into the model. Based on the methodology of this particular laser ceilometer a minimum threshold for cloud detectability, α_{min}, was then inferred to determine the presence of clouds. Using this threshold, specific atmospheric conditions were modeled. Results demonstrated that certain atmospheric conditions, such as large concentrations of background aerosols, could exist such that, some cloud types would not be identified by the laser ceilometer.

APPENDIX A-1. PHASE FUNCTIONS USED FOR COMPARISONS

The phase functions listed, which are normalized to 4π, were used for comparing the current model with previously published model results.

A. Haze C, λ = 0.70 μm (Kunkel, 1972)

ANGLE	PHASE FCN ($P(\theta)/4\pi$)
0	2.5
5	1.9
10	1.2
15	0.8
20	0.6
25	0.4
30	0.29
35	0.2
40	0.15
45	0.11
50	0.085
55	0.065
60	0.049
65	0.0385
70	0.03
75	0.0235
80	0.019
85	0.01555
90	0.0139
95	0.01215
100	0.01075
105	0.00985
110	0.009
115	0.0086
120	0.0085
125	0.00875
130	0.00905
135	0.009555
140	0.0106
145	0.0115
150	0.01235
155	0.013
160	0.01325
165	0.014
170	0.014
175	0.01275
180	0.016

B. Nimbostratus, λ = 0.70 μm (Smith, 1987)

ANGLE	PHASE FCN	ANGLE	PHASE FCN
0	886.9	25.94	0.235
0.01978	886.9	27.06	0.21915
0.07133	877	28.21	0.20385
0.14935	842.5	29.37	0.1893
0.25023	764.15	30.55	0.17555
0.38001	627.15	31.74	0.1625
0.53995	446.6	32.96	0.1501
0.73008	265.15	34.2	0.1385
0.94998	131.05	35.45	0.1274
1.1899	59.1	36.71	0.11685
1.4601	28.715	38	0.1071
1.76	15.995	39.3	0.097965
2.08	9.7	40.62	0.08939
2.44	6.2435	41.95	0.08142
2.81	4.2405	43.3	0.07397
3.22	3.025	44.66	0.067135
3.65	2.2605	46.03	0.06054
4.11	1.763	47.42	0.05473
4.6	1.4285	48.82	0.0493
5.12	1.198	50.24	0.0443
5.65	1.035	51.67	0.03965
6.22	0.9172	53.1	0.035355
6.81	0.82835	54.55	0.031565
7.43	0.75995	56.02	0.028085
8.07	0.706	57.49	0.0249
8.74	0.662	58.97	0.02201
9.43	0.62475	60.46	0.019375
10.15	0.59255	61.96	0.017065
10.9	0.5638	63.47	0.01503
11.66	0.53755	64.99	0.01318
12.46	0.51305	66.51	0.01153
13.27	0.4895	68.05	0.010062
14.11	0.46725	69.59	0.0087985
14.97	0.44545	71.13	0.0076895
15.86	0.42425	72.68	0.006716
16.77	0.40325	74.24	0.0058515
17.7	0.38285	75.8	0.0051065
18.66	0.3628	77.37	0.004482
19.63	0.3432	78.94	0.003951
20.63	0.3237	80.51	0.003492
21.65	0.3047	82.09	0.0030935
22.69	0.2865	83.67	0.002767
23.76	0.2688	85.25	0.0025005
24.84	0.25165	86.83	0.002269

B (continued). Nimbostratus, λ = 0.70 μm

ANGLE	PHASE FCN	ANGLE	PHASE FCN
88.42	0.0020795	152.94	0.011125
90	0.0019185	154.06	0.01076
91.58	0.0017915	155.16	0.01042
93.17	0.001695	156.24	0.010105
94.75	0.001614	157.31	0.0099255
96.33	0.0015621	158.35	0.009535
97.91	0.001524	159.37	0.0093795
99.49	0.0015015	160.37	0.009179
101.06	0.0014908	161.34	0.009002
102.63	0.001494	162.3	0.008839
104.2	0.001514	163.23	0.008695
105.76	0.0015445	164.14	0.008592
107.32	0.001594	165.03	0.0085135
108.87	0.0016565	165.89	0.0084345
110.41	0.0017255	166.73	0.0083875
111.95	0.001802	167.54	0.008378
113.49	0.0018595	168.34	0.008399
115.01	0.0019085	169.1	0.008402
116.53	0.002023	169.85	0.0085505
118.04	0.00228	170.57	0.0086055
119.54	0.0027465	171.26	0.00873
121.03	0.003329	171.93	0.0089425
122.51	0.0038545	172.57	0.0091515
123.98	0.004185	173.19	0.0094095
125.45	0.0042625	173.78	0.0097935
126.9	0.004089	174.35	0.010253
128.33	0.0037555	174.88	0.010794
129.76	0.003457	175.4	0.011435
131.18	0.0033495	175.89	0.012262
132.58	0.0036295	176.35	0.013296
133.97	0.0046485	176.78	0.014525
135.34	0.0069675	177.19	0.01624
136.7	0.011204	177.56	0.018525
138.05	0.017455	177.92	0.02146
139.38	0.024248	178.24	0.02537
140.7	0.028168	178.54	0.02997
142	0.026204	178.81	0.03281
143.29	0.019827	179.05	0.031045
144.55	0.014415	179.27	0.027585
145.8	0.012815	179.46	0.028945
147.04	0.013075	179.62	0.0362
148.26	0.013	179.75	0.044885
149.45	0.01249	179.85	0.0509
150.63	0.01196	179.93	0.053775
151.79	0.011535	179.98	0.05462
		180	0.05462

APPENDIX A-2. PHASE FUNCTIONS USED IN CURRENT WORK

The phase functions listed were used in obtaining the results discussed in this paper, and were generated using a separate program (MIECODE, Eric A. Smith, Dept. of Atmos. Science, Colorado State University, Fort Collins, CO). The integration of the phase functions over a sphere equals 4π.

A. Haze L, λ = 0.90 μm (background aerosol approximation)

ANGLE	PHASE FCN	ANGLE	PHASE FCN
0	1.917	16.77	0.8626
0.02	1.917	17.7	0.804
0.07	1.916	18.66	0.7474
0.15	1.916	19.63	0.6932
0.25	1.916	20.63	0.6414
0.38	1.915	21.65	0.5922
0.54	1.914	22.69	0.5457
0.73	1.913	23.76	0.502
0.95	1.91	24.84	0.4609
1.19	1.907	25.94	0.4226
1.46	1.902	27.06	0.3869
1.76	1.895	28.21	0.3538
2.08	1.886	29.37	0.3232
2.44	1.875	30.55	0.2949
2.81	1.862	31.74	0.2689
3.22	1.845	32.96	0.245
3.65	1.825	34.2	0.2232
4.11	1.802	35.45	0.2033
4.6	1.775	36.71	0.1851
5.12	1.745	38	0.1685
5.65	1.71	39.3	0.1535
6.22	1.671	40.62	0.1398
6.81	1.628	41.95	0.1273
7.43	1.582	43.3	0.1161
8.07	1.531	44.66	0.1058
8.74	1.478	46.03	0.09658
9.43	1.421	47.42	0.0882
10.15	1.362	48.82	0.08062
10.9	1.301	50.24	0.07377
11.66	1.239	51.67	0.06756
12.46	1.175	53.1	0.06194
13.27	1.111	54.55	0.05685
14.11	1.048	56.02	0.05224
14.97	0.9849	57.49	0.04806
15.86	0.923	58.97	0.04429

A (continued). Haze L, λ = 0.90 μm

ANGLE	PHASE FCN	ANGLE	PHASE FCN
60.46	0.04087	129.76	0.007816
61.96	0.03777	131.18	0.007886
63.47	0.03496	132.58	0.007968
64.99	0.03241	133.97	0.008058
66.51	0.03009	135.34	0.008157
68.05	0.02798	136.7	0.008264
69.59	0.02606	138.05	0.00838
71.13	0.02432	139.38	0.008506
72.68	0.02274	140.7	0.008639
74.24	0.0213	142	0.008777
75.8	0.01999	143.29	0.008915
77.37	0.01879	144.55	0.009051
78.94	0.0177	145.8	0.009182
80.51	0.0167	147.04	0.009307
82.09	0.01579	148.26	0.009427
83.67	0.01496	149.45	0.009541
85.25	0.0142	150.63	0.009649
86.83	0.01351	151.79	0.009747
88.42	0.01288	152.94	0.00983
90	0.0123	154.06	0.009894
91.58	0.01178	155.16	0.009934
93.17	0.0113	156.24	0.009948
94.75	0.01086	157.31	0.009935
96.33	0.01046	158.35	0.009897
97.91	0.01009	159.37	0.009834
99.49	0.009764	160.37	0.009748
101.06	0.009465	161.34	0.009642
102.63	0.009195	162.3	0.009517
104.2	0.008952	163.23	0.009373
105.76	0.008734	164.14	0.009212
107.32	0.008539	165.03	0.009039
108.87	0.008367	165.89	0.008858
110.41	0.008217	166.73	0.008676
111.95	0.008086	167.54	0.008501
113.49	0.007975	168.34	0.008342
115.01	0.007881	169.1	0.008209
116.53	0.007805	169.85	0.008106
118.04	0.007746	170.57	0.00804
119.54	0.007703	171.26	0.008013
121.03	0.007677	171.93	0.008023
122.51	0.007666	172.57	0.008068
123.98	0.007668	173.19	0.008144
125.45	0.007684	173.78	0.008242
126.9	0.007714	174.35	0.008358
128.33	0.007758	174.88	0.008483

A (continued). Haze L, λ = 0.90 μm

ANGLE	PHASE FCN	ANGLE	PHASE FCN
175.4	0.008611	179.05	0.009376
175.89	0.008737	179.27	0.009394
176.35	0.008856	179.46	0.009406
176.78	0.008965	179.62	0.009413
177.19	0.009062	179.75	0.009418
177.56	0.009145	179.85	0.00942
177.92	0.009215	179.93	0.009421
178.24	0.009272	179.98	0.009421
178.54	0.009317	180	0.009421
178.81	0.009351		

B. Nimbostratus, λ = 0.90 μm

ANGLE	PHASE FCN	ANGLE	PHASE FCN
0	462.9	15.86	0.43115
0.01978	462.9	16.77	0.4089
0.07133	459.8	17.7	0.38715
0.14935	448.9	18.66	0.366
0.25023	423.8	19.63	0.3455
0.38001	377.1	20.63	0.32545
0.53995	308.55	21.65	0.30595
0.73008	226.35	22.69	0.2872
0.94998	147.15	23.76	0.269
1.1899	86.39	24.84	0.2516
1.4601	48.66	25.94	0.2345
1.76	28.04	27.06	0.21865
2.08	16.71	28.21	0.20325
2.44	10.175	29.37	0.1886
2.81	6.408	30.55	0.17475
3.22	4.2715	31.74	0.1617
3.65	3.041	32.96	0.1492
4.11	2.292	34.2	0.13755
4.6	1.807	35.45	0.12645
5.12	1.4755	36.71	0.1162
5.65	1.2415	38	0.1064
6.22	1.0715	39.3	0.097355
6.81	0.94525	40.62	0.0889
7.43	0.8499	41.95	0.08101
8.07	0.7757	43.3	0.073695
8.74	0.71635	44.66	0.066905
9.43	0.6677	46.03	0.060665
10.15	0.6266	47.42	0.054835
10.9	0.59095	48.82	0.049475
11.66	0.5591	50.24	0.04457
12.46	0.53025	51.67	0.04008
13.27	0.5037	53.1	0.035955
14.11	0.4783	54.55	0.032185
14.97	0.4544	56.02	0.028765

B (continued). Nimbostratus, λ = 0.90 μm

ANGLE	PHASE FCN	ANGLE	PHASE FCN
57.49	0.02564	129.76	0.004172
58.97	0.022825	131.18	0.0044935
60.46	0.020285	132.58	0.0052715
61.96	0.017985	133.97	0.0067525
63.47	0.015945	135.34	0.0092615
64.99	0.0141	136.7	0.01293
66.51	0.012455	138.05	0.017522
68.05	0.010999	139.38	0.02198
69.59	0.0097035	140.7	0.024586
71.13	0.0085685	142	0.024051
72.68	0.0075565	143.29	0.020709
74.24	0.006671	144.55	0.016745
75.8	0.0059045	145.8	0.014127
77.37	0.005235	147.04	0.012985
78.94	0.0046545	148.26	0.01264
80.51	0.004146	149.45	0.01221
82.09	0.0037135	150.63	0.011865
83.67	0.0033455	151.79	0.01157
85.25	0.0030305	152.94	0.01132
86.83	0.0027565	154.06	0.011065
88.42	0.00253	155.16	0.010885
90	0.0023415	156.24	0.010615
91.58	0.0021845	157.31	0.0104
93.17	0.002056	158.35	0.010234
94.75	0.00195	159.37	0.010084
96.33	0.001869	160.37	0.0098495
97.91	0.001808	161.34	0.009784
99.49	0.0017665	162.3	0.009735
101.06	0.00174	163.23	0.009657
102.63	0.0017255	164.14	0.009573
104.2	0.001725	165.03	0.0095645
105.76	0.001736	165.89	0.009585
107.32	0.001766	166.73	0.009626
108.87	0.0018095	167.54	0.0097495
110.41	0.001862	168.34	0.0099315
111.95	0.0019265	169.1	0.01007
113.49	0.0020095	169.85	0.010168
115.01	0.0021345	170.57	0.010407
116.53	0.0023325	171.26	0.010778
118.04	0.0026205	171.93	0.011122
119.54	0.002996	172.57	0.011519
121.03	0.00339	173.19	0.012045
122.51	0.003729	173.78	0.01278
123.98	0.003961	174.35	0.013653
125.45	0.004069	174.88	0.01465
126.9	0.004091	175.4	0.016015
128.33	0.0040885	175.89	0.017775

B (continued). Nimbostratus, λ = 0.90 μm

ANGLE	PHASE FCN	ANGLE	PHASE FCN
176.35	0.019965	179.27	0.030895
176.78	0.02252	179.46	0.03586
177.19	0.02518	179.62	0.042475
177.56	0.027675	179.75	0.0481
177.92	0.029935	179.85	0.05146
178.24	0.031925	179.93	0.05298
178.54	0.03273	179.98	0.05341
178.81	0.03145	180	0.05341
179.05	0.029745		

C. Stratus, λ = 0.90 μm

ANGLE	PHASE FCN	ANGLE	PHASE FCN
0	124.2	16.77	0.41735
0.02	124.2	17.7	0.39315
0.07	124	18.66	0.37035
0.15	123.2	19.63	0.34865
0.25	121.5	20.63	0.32765
0.38	118	21.65	0.3071
0.54	112.15	22.69	0.28755
0.73	103.4	23.76	0.26885
0.95	91.645	24.84	0.2512
1.19	77.395	25.94	0.23445
1.46	61.78	27.06	0.2182
1.76	46.405	28.21	0.20265
2.08	32.77	29.37	0.1876
2.44	21.9	30.55	0.17385
2.81	14.07	31.74	0.1611
3.22	8.9155	32.96	0.14875
3.65	5.7575	34.2	0.13705
4.11	3.8985	35.45	0.1259
4.6	2.8065	36.71	0.11585
5.12	2.1425	38	0.1066
5.65	1.7145	39.3	0.0977
6.22	1.4215	40.62	0.08929
6.81	1.21	41.95	0.081605
7.43	1.052	43.3	0.074805
8.07	0.9307	44.66	0.068145
8.74	0.83555	46.03	0.06195
9.43	0.7595	47.42	0.05637
10.15	0.69745	48.82	0.05134
10.9	0.64565	50.24	0.046505
11.66	0.60135	51.67	0.042075
12.46	0.56275	53.1	0.038195
13.27	0.52815	54.55	0.034445
14.11	0.4968	56.02	0.031135
14.97	0.4688	57.49	0.02806
15.86	0.4427	58.97	0.025335

C (continued). Stratus, λ = 0.90 μm

ANGLE	PHASE FCN	ANGLE	PHASE FCN
60.46	0.022725	131.18	0.0061275
61.96	0.02053	132.58	0.0072005
63.47	0.01841	133.97	0.0086945
64.99	0.01655	135.34	0.01053
66.51	0.014875	136.7	0.012679
68.05	0.013365	138.05	0.015134
69.59	0.01199	139.38	0.017563
71.13	0.01077	140.7	0.019546
72.68	0.009704	142	0.020849
74.24	0.0086765	143.29	0.021146
75.8	0.0078395	144.55	0.020449
77.37	0.0070645	145.8	0.018879
78.94	0.006345	147.04	0.016972
80.51	0.005768	148.26	0.015112
82.09	0.0052525	149.45	0.013585
83.67	0.0047645	150.63	0.012655
85.25	0.0043795	151.79	0.01223
86.83	0.004042	152.94	0.012115
88.42	0.00372	154.06	0.012145
90	0.003445	155.16	0.01225
91.58	0.0032145	156.24	0.01227
93.17	0.003001	157.31	0.01224
94.75	0.0028365	158.35	0.01216
96.33	0.002688	159.37	0.012115
97.91	0.0025705	160.37	0.01218
99.49	0.0024845	161.34	0.01216
101.06	0.002389	162.3	0.012165
102.63	0.0023255	163.23	0.012255
104.2	0.0022925	164.14	0.012365
105.76	0.002274	165.03	0.012515
107.32	0.0022995	165.89	0.01271
108.87	0.0023585	166.73	0.013035
110.41	0.00246	167.54	0.01339
111.95	0.0026205	168.34	0.01376
113.49	0.0027635	169.1	0.014275
115.01	0.0029565	169.85	0.01494
116.53	0.003176	170.57	0.01566
118.04	0.003385	171.26	0.016325
119.54	0.003556	171.93	0.01695
121.03	0.0037595	172.57	0.01785
122.51	0.00384	173.19	0.01932
123.98	0.0040175	173.78	0.021395
125.45	0.0041995	174.35	0.023975
126.9	0.004437	174.88	0.02708
128.33	0.0047735	175.4	0.030635
129.76	0.0053925	175.89	0.034325

C (continued). Stratus, λ = 0.90 μm

ANGLE	PHASE FCN	ANGLE	PHASE FCN
176.35	0.037425	179.27	0.040665
176.78	0.038995	179.46	0.044675
177.19	0.038395	179.62	0.047645
177.56	0.035845	179.75	0.04952
177.92	0.032525	179.85	0.05049
178.24	0.030125	179.93	0.050895
178.54	0.02992	179.98	0.05101
178.81	0.03219	180	0.05101
179.05	0.03616		

D. Cumulus, λ = 0.90 μm

ANGLE	PHASE FCN	ANGLE	PHASE FCN
0	83.55	16.77	0.4216
0.02	83.55	17.7	0.397
0.07	83.46	18.66	0.37345
0.15	83.14	19.63	0.35115
0.25	82.37	20.63	0.3297
0.38	80.81	21.65	0.3087
0.54	78.155	22.69	0.2888
0.73	74.065	23.76	0.26975
0.95	68.345	24.84	0.25135
1.19	61.01	25.94	0.2341
1.46	52.32	27.06	0.2176
1.76	42.865	28.21	0.2017
2.08	33.4	29.37	0.18695
2.44	24.72	30.55	0.17315
2.81	17.435	31.74	0.1601
3.22	11.82	32.96	0.1477
3.65	7.8345	34.2	0.13635
4.11	5.207	35.45	0.12565
4.6	3.567	36.71	0.11555
5.12	2.572	38	0.10635
5.65	1.9665	39.3	0.097725
6.22	1.583	40.62	0.08958
6.81	1.3255	41.95	0.08216
7.43	1.1405	43.3	0.075275
8.07	0.9995	44.66	0.06879
8.74	0.88885	46.03	0.06287
9.43	0.8001	47.42	0.057405
10.15	0.7281	48.82	0.05229
10.9	0.66905	50.24	0.04763
11.66	0.6199	51.67	0.043345
12.46	0.57785	53.1	0.03933
13.27	0.54055	54.55	0.035745
14.11	0.50675	56.02	0.03238
14.97	0.47575	57.49	0.029315
15.86	0.4475	58.97	0.02655

C (continued). Cumulus, λ = 0.90 μm

ANGLE	PHASE FCN	ANGLE	PHASE FCN
60.46	0.02397	131.18	0.0068165
61.96	0.02166	132.58	0.0078855
63.47	0.01955	133.97	0.0092855
64.99	0.017615	135.34	0.010955
66.51	0.01591	136.7	0.012839
68.05	0.01431	138.05	0.01487
69.59	0.01292	139.38	0.016929
71.13	0.01165	140.7	0.018662
72.68	0.010486	142	0.019918
74.24	0.0095015	143.29	0.020648
75.8	0.008568	144.55	0.020501
77.37	0.007776	145.8	0.019584
78.94	0.0070565	147.04	0.01839
80.51	0.0064155	148.26	0.016718
82.09	0.0058625	149.45	0.015163
83.67	0.0053605	150.63	0.013995
85.25	0.0049285	151.79	0.013105
86.83	0.004539	152.94	0.01265
88.42	0.004205	154.06	0.01258
90	0.0038915	155.16	0.012615
91.58	0.003633	156.24	0.012675
93.17	0.003393	157.31	0.012835
94.75	0.0031805	158.35	0.013065
96.33	0.0030115	159.37	0.01302
97.91	0.0028575	160.37	0.01296
99.49	0.0027375	161.34	0.013025
101.06	0.0026525	162.3	0.01306
102.63	0.0025945	163.23	0.01325
104.2	0.0025645	164.14	0.013545
105.76	0.0025795	165.03	0.01374
107.32	0.0026195	165.89	0.013925
108.87	0.0026905	166.73	0.01423
110.41	0.002801	167.54	0.014685
111.95	0.0029325	168.34	0.015365
113.49	0.0030765	169.1	0.01622
115.01	0.003246	169.85	0.01707
116.53	0.0034125	170.57	0.01789
118.04	0.003566	171.26	0.01875
119.54	0.00374	171.93	0.019725
121.03	0.003884	172.57	0.02098
122.51	0.00406	173.19	0.022825
123.98	0.004264	173.78	0.025465
125.45	0.0044965	174.35	0.028845
126.9	0.0048675	174.88	0.032595
128.33	0.0053105	175.4	0.03607
129.76	0.0059495	175.89	0.03848

C (continued). Cumulus, λ = 0.90 μm

ANGLE	PHASE FCN	ANGLE	PHASE FCN
176.35	0.03913	179.27	0.044625
176.78	0.037815	179.46	0.04778
177.19	0.035105	179.62	0.04997
177.56	0.032175	179.75	0.051305
177.92	0.030355	179.85	0.05198
178.24	0.030525	179.93	0.052265
178.54	0.032755	179.98	0.05234
178.81	0.036445	180	0.05234
179.05	0.04068		

REFERENCES

Allen, R. J., and C. M. R. Platt, 1977: Lidar for multiple backscattering and depolarization observations. *Appl. Opt.*, 16, 3193-3199.

Bissonnette, L. R., 1988: Multiscattering model for propagation of narrow light beams in aerosol media. *Appl. Opt.*, 27, 2478-2484.

Carrier, L. W., G. A. Cato, and K. J. von Essen, 1967: The backscattering and extinction of visible and infrared radiation by selected major cloud models. *Appl. Opt.*, 6, 1209-1216.

Collins, D. G., and M. B. Wells, 1965: Monte Carlo codes for study of light transport in the atmosphere, Vol. 1. Report RRA-T54 (Radiation Research Associates, Inc., Fort Worth, Texas).

Collins, D. G., and M. B. Wells, 1970: FLASH, A Monte Carlo procedure for use in calculating light scattering in a spherical-shell atmosphere. Report RRA-T704 (Radiation Research Associates, Inc., Fort Worth, Texas).

Collins, D. G., W. G. Blattner, M. B. Wells, and H. G. Horak, 1972: Backward Monte Carlo calculations of the polarization characteristics of the radiation emerging from spherical-shell atmospheres. *Appl. Opt.*, 11, 2684-2696.

Davis, J. M., S. K. Cox, and T. B. McKee, 1979a: Total shortwave radiative characteristics of absorbing finite clouds. *J. Atmos. Sci.*, 36, 508-518.

Davis, J. M., S. K. Cox, and T. B. McKee, 1979b: Vertical and horizontal distributions of solar absorption in finite clouds. *J. Atmos. Sci.*, 36, 1976-1984.

Davis, J. M., T. B. McKee, and S. K. Cox, 1985: Application of the Monte Carlo method to problems in visibility using a local estimate: an investigation. *Appl. Opt.*, 24, 3193-3204.

Deirmendjian, D., 1969: **Electromagnetic Scattering on Spherical Polydispersions**, Elsevier, 290 pp.

Deirmendjian, D., 1975: Far infrared and submillimeter wave attenuation by clouds and rain. *J. Appl. Meteor.*, 14, 1584-1593.

Eloranta, E. W., 1972: Calculation of doubly scattered lidar returns. PhD thesis, University of Wis.

Elterman, L., 1968: UV, visible, and IR attenuation for altitudes to 50 Km, Technical Report AFCRL-68-0153.

Kattawar, G. W., and G. N. Plass, 1968a: Radiance and polarization of multiple scattered light from haze and clouds. *Appl. Opt.*, 7, 869-878.

Kattawar, G. W., and G. N. Plass, 1968b: Radiance and polarization of multiple scattered light from haze and clouds. *Appl. Opt.*, 7, 1519-1527.

Kunkel, K. E., 1974: Monte Carlo analysis of multiply scattered lidar returns. M.S. thesis, Dept. of Meteorology, University of Wisconsin, 91 pp.

Kunkel, K. E., and J. A. Weinman, 1976: Monte Carlo analysis of multiply scattered lidar returns. *J. Atmos. Sci.*, 33, 1772-1781.

Lenoble, J., Ed., 1985: **Radiative Transfer in Scattering and Absorbing Atmospheres: Standard Computational Procedures**, A. Deepak, 300 pp.

Liou, K., and R. M. Schotland, 1971: Multiple backscattering and depolarization from water clouds for a pulsed laser. *J. Atmos. Sci.*, 28, 772-784.

Liou, K., and R. M. Schotland, 1971: Time-Dependent multiple backscattering. *J. Atmos. Sci.*, 28, 824-827.

McKee, T. B., and S. K. Cox, 1974: Scattering of visible radiation by finite clouds. *J. Atmos. Sci.*, 31, 1885-1892.

McKee, T. B., and S. K. Cox, 1976: Simulated radiance patterns for finite cubic clouds. *J. Atmos. Sci.*, 33, 2014-2020.

McKee, T. B., M. DeMaria, J. A. Kuenning, and S. K. Cox, 1983: Comparison of Monte Carlo calculations with observations of light scattering in finite clouds. *J. Atmos. Sci.*, 40, 1016-1023.

Measures, R. M., 1983: **Laser Remote Sensing: Fundamentals and Applications**, John Wiley and Sons, 483 pp.

Ouldridge, M., D. W. Jones, and D. J. Painting, 1989: The WMO international ceilometer intercomparison, Beaufort Park 1986. *Meteor. Magazine*, 118, 242-246.

Pal, S. R., and A. I. Carswell, 1976: Multiple scattering in atmospheric clouds: lidar observations. *Appl. Opt.*, 15, 1990-1995.

Plass, G. N., and G. W. Kattawar, 1968a: Influence of single scattering albedo on reflected and transmitted light from clouds. *Appl. Opt.*, 7, 361-367.

Plass, G. N., and G. W. Kattawar, 1968b: Monte Carlo calculations of light scattering from clouds. *Appl. Opt.*, 7, 415-419.

Plass, G. N., and G. W. Kattawar, 1968c: Radiant intensity of light scattered from clouds. *Appl. Opt.*, 7, 699-704.

Plass, G. N., and G. W. Kattawar, 1968d: Calculations of reflected and transmitted radiance for earth's atmosphere. *Appl. Opt.*, 7, 1129-1135.

Plass, G. N., and G. W. Kattawar, 1970: Polarization of the radiation reflected and transmitted by the earth's atmosphere. *Appl. Opt.*, 9, 1122-1125.

Plass, G. N., and G. W. Kattawar, 1971: Reflection of light pulses from clouds. *Appl. Opt.*, 10, 2304-2310.

Plass, G. N., and G. W. Kattawar, 1971: Reflection of light pulses from clouds. *Appl. Opt.*, 10, 2304-2310.

Platt, C. M. R., 1979: Remote sounding of high clouds: I. Calculation of visible and infrared optical properties from lidar and radiometer measurements. *J. Appl. Meteor.*, 18, 1130-1143.

Platt, C. M. R., and A. C. Dilley, 1979: Remote sounding of high clouds: II. Emmissivity of cirrostratus. *J. Appl. Meteor.*, 18, 1144-1150.

Platt, C. M. R., 1981: Remote sounding of high clouds: III. Monte Carlo calculations of multiple scattered lidar returns. *J. Atmos. Sci.*, 38, 156-167.

Tsay, S. C., J. M. Davis, G. L. Stephens, S. K. Cox, and T. B. McKee, 1987: Backward Monte Carlo computations of radiation propagating in horizontally inhomogeneous media. Part I: Description of Codes, CIRA report, Fort Collins, Colorado, 76 pp.

Wiegner, M. and G. Echle, 1992: A model for lidar multiple scattering. *Proceedings of the International Radiation Symposium*, 469-472.

Weinman, J. A., 1976: Effects of multiple scattering on light pulses reflected by turbid atmospheres. *J. Atmos. Sci.*, 33, 1763-1771.

Weissbluth, W. J., J. M. Davis, and S. K. Cox, 1987: A modeling study of visibility in the Grand Canyon, *Atmos. Environ.*, 21, 703-713.

Welch, R. M., S. K. Cox, and J. M. Davis, 1980: Solar Radiation and Clouds, *Meteor. Monographs.*, 17, No. 39, Amer. Met. Soc., Boston, MA